Robotic Fiber Positioning Systems for Massive Spectroscopic Surveys:
Mechanical Design Guidelines and Technological Opportunities

PAR

Philipp HÖRLER

ÉCOLE POLYTECHNIQUE
FÉDÉRALE DE LAUSANNE

Suisse
2018

Acknowledgments

I would like to thank my supervisors Hannes Bleuler, Jean-Paul Kneib and Mohamed Bouri. They strongly encouraged and inspired me to explore new solutions and supported me in the exploration of my research. I am grateful also to my defence jury members Dimitris Kiritsis, Michael Schubnell, Luca Pasquini and Yves Bellouard for their great suggestions to improve my works. A big thank you also to the mechanical workshops ATME and ATPR, specifically Marc Jeanneret and Alfred Thomas, without who the realization of our prototypes would not have been possible and who were very available to support us at all times.

I would also like to thank all the colleagues and friends who made my time at EPFL a nice one. Thanks also to my family and to my one and only Claudia who supported and put up with me during this time.

"Was mus me mache?" - Rafael Gort

Abstract

The technology of fiber positioning robots has been evolving in the recent years and currently lacks of a comprehensive view. This thesis aims at filling this gap. Fiber positioning robots are analyzed under different aspects: a theoretical framework, design guidelines and a discussion on the limits of the technology are provided. Furthermore, a detailed description of two robots that we have implemented is given, together with the related performance results.

The theoretical framework and the design guidelines can be a tool for future work on fiber positioners. The smallest robot we have developed is at the technological frontier and represents a novelty in the state of the art.

Keywords Fiber positioning robots, Spectroscopic surveys, Mechanical design, Calibration, High-precision mechanics, Micro motors

Kurzfassung

Die Technologie der faserpositionierenden Roboter hat in den letzten Jahren erhebliche Fortschritte gemacht. Es fehlt jedoch eine umfassende Studie. Diese Arbeit hat das Ziel diese Lücke zu füllen. Faserpositionierende Roboter werden aus verschiedenen Blickwinkeln analysiert: Ein theoretischer Rahmen wird präsentiert, Konstruktionsrichtlinien werden vorgeschlagen und die Grenzen dieser Technologie werden diskutiert. Ausserdem wird eine detailierte Beschreibung zweier unserer Roboter inklusive Leistungsergebnisse gegeben.

Der theoretische Rahmen und die Konstruktionsrichtlinien können ein Instrument für zukünftige Arbeit mit faserpositionierenden Roboter sein. Der kleinste Roboter den wir entwickelt haben is an der Grenze des Möglichen und eine Neuheit im Stand der Technik.

Stichworte Faserpositionierende Roboter, Spektroskopische Studien, Maschinenbau, Kalibration, Präzisionsmechanik, Miniaturmotoren

Contents

List of Figures

8

9

List of Tables

Definitions

Multi object spectroscopy (MOS) An astronomic observation strategy where the spectra of multiple objects are measured simultaneously. This can be achieved in various ways: using a slit mask, multiple optical fibers or micro mirror arrays.

Fiber positioning system A system capable of individually placing optical fibers or fiber bundles in the focal plane of a telescope.

Fiber positioner A robotic device capable of placing one optical fiber or fiber bundle in the focal plane of a telescope. Usually part of a fiber positioning system.

Precision A description of random errors. Also called repeatability. If a precise positioning device is commanded to the same target multiple times, it has a low variance in the attained positions.

Accuracy A description of systematic errors. If an accurate positioning device is commanded to the same target multiple times, the average of the attained positions is close to the true target.

Alpha, Beta axis In the case of the SCARA-like kinematics we refer to the first axis as the Alpha axis, and the second axis as the Beta axis. Idem for the Alpha arm and Beta arm. Alpha and Beta alone are the angles of the Alpha and Beta arms, defining the position of the positioner. Refer to figure 4.1.

Axis An axis is a geometric line that is the center of rotation of a body.

Backlash Backlash is the clearance between the teeth of reduction gears which causes the output to be uncontrollable while the gears are not in contact.

Hysteresis In general, hysteresis is the dependence of the state of a system on its history. In the case of the fiber positioners we define the hysteresis the difference in position when approaching a target from different directions. The hysteresis is due to backlash, friction and deformation of parts of the drivetrain.

Chapter 1

Introduction

In various astrophysical science cases, a large number of light spectra of diverse astronomical objects (stars, galaxies and quasars of different magnitudes) have to be observed in parallel. The information extracted from light spectra (e.g. redshift, relative velocities, chemical composition, and imprint of the intergalactic medium in the line of sight of quasars) helps to better understand the history and evolution of our Universe, the formation of stars and galaxies and the mystery dark energy. In the context of these science cases the used spectra are in the visible to near-infrared range (0.36 to 1.8 μm) and a resolution of $R = 1000$ to $20'000$ is needed.

In order to capture light spectra, optical fibers are used as shown if figure 1.1. They transmit the light of observed objects from the focal plane of a telescope to a spectrograph. The fibers have to be located in the focal plane where the object to observe is projected. One fiber collects the light of one object, so the number of fibers is be equal to the number of observed objects. The use of robots to position the fibers allows to reach a high accuracy while keeping a short reconfiguration time. The required precision in the placement of the fibers is around 5 to 20 μm and the reconfiguration time in the order of one minute.

An example of science case where fiber positioners are used is the measurement of large-scale structures in the universe via the baryonic acoustic oscillation peak [12], which can be found in the distribution of galaxies [3, 2] and in the Ly-α forest of distant quasars [9]. The BOSS spectrograph on the Sloan Telescope was the instrument that had been employed for this science case (Sloan Digital Sky Survey - SDSS). The BOSS spectrograph was based on manual plugging of fibers in aluminium plates in the focal plane of the telescope, which takes several hours. The important discoveries achieved with this survey showed the need to increase the number of objects to be observed. This has triggered the development of new massive spectroscopic instruments with a higher density of fibers and a shorter reconfiguration time, achieved thanks to the use of robotized fiber positioners.
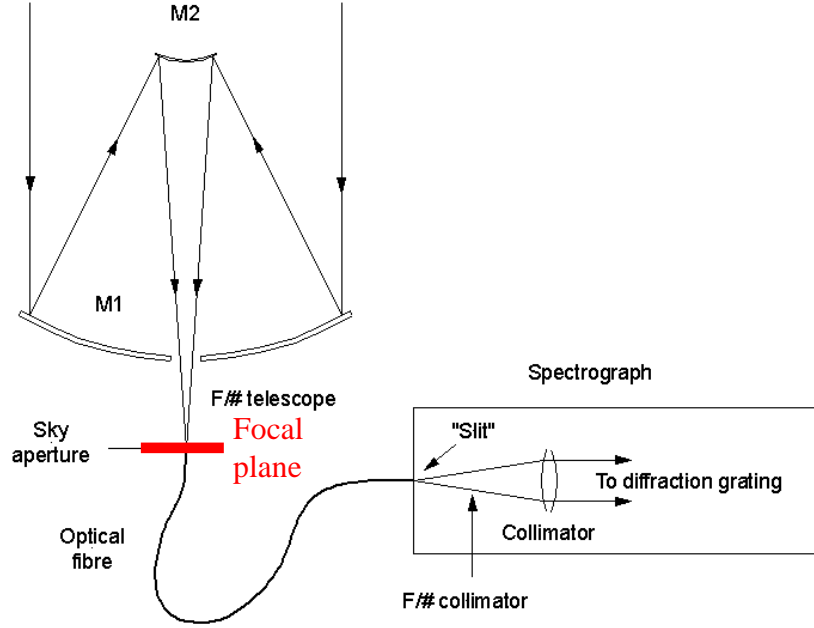
Figure 1.1: Principle of fiber based spectroscopy. Light is gathered by the telescope, transmitted by optical fibers and analyzed by a spectrograph. Image source: https://spectroscopy.wordpress.com

The first high-density robotized positioning systems to place all the fibers in a coordinated way at the targeted positions were the Large Sky Area Multi-Object fiber Spectroscopic Telescope (LAMOST) [47] and the Fiber Multi-Object Spectrograph (FMOS) [27]. However, these two systems initially suffered of some limitations due to lack of accuracy and long reconfiguration time.

The most recent wave of projects, which will be ready in the next few years, such as the Prime Focus Spectrograph (PFS) [46, 16], the Multi-Object Optical and Nearinfrared Spectrograph (MOONS) [6], the Dark Energy Spectroscopic Instrument (DESI) [18, 43] and the 4-metre Multi-Object Spectroscopic Telescope (4MOST) [8] have been making rapid progress in the direction of improved accuracy and reconfiguration time. They all use robotized positioning systems with 1000 to 5000 fibers. The main goal is to conduct spectroscopy on a large number of objects (1-50 million) over a wide field of view (from 0.15 to 7 square degrees) within a reasonable amount of time, thus opening new science opportunities for galactic and extragalactic spectroscopic surveys.

Planned future projects will need smaller positioners to accommodate up to 20'000 fibers. The current challenge is to push the technology at the limit in terms of robot size and to assure reliable mass production of robots. Different variants of robots are competing and the community has not yet settled on the best strategy

for MOS [10].

The objective of this thesis is to provide a comprehensive mechanical investigation of the challenges related to fiber positioning robots. This thesis presents a theoretical framework, design guidelines, an exploration of the technological limits and the description of two robots that we have prototyped. The theoretical framework derives the mechanical characteristics that a fiber positioner has to respect from the related astrophysical needs. On the basis of these characteristics, guidelines for the design of fiber positioners are provided.
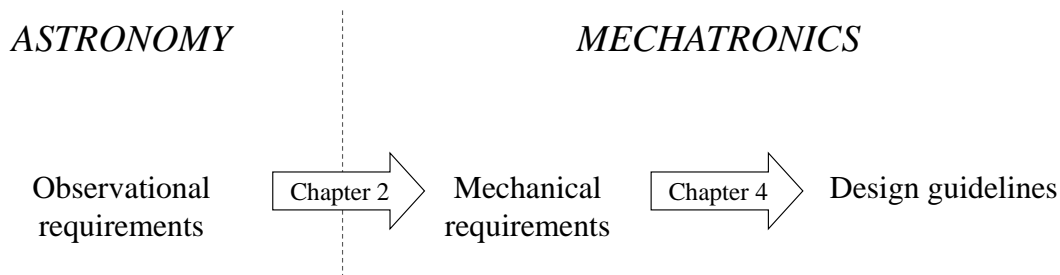
Figure 1.2: Chapter 2 makes the link between astronomy and mechatronics while chapter 4.1 details mechanical design guidelines based on the mechanical requirements.

Given the necessity to develop the smallest possible positioners, a discussion on the possibility to reduce the size of positioners is given. In this context, two robots have been developed, one with a diameter of 25mm and another with a diameter of 7mm, both characterized by high accuracy and short reconfiguration time, the latter being at the technological frontier regarding minimal size. The thesis is structured as follows: chapter 2 defines the requirements for a fiber positioner system and gives a rationale for each of them starting from each astrophysical need. In chapter 3, the existing solutions for multi object spectroscopy are presented and compared. Chapter 4 gives design guidelines for fiber positioners and discusses the limits and opportunities of their application. Finally, chapter 5 presents the development of the two fiber positioners and chapter 6 their performance results.

Chapter 2

From observational objectives to mechanical requirements

This chapter defines the requirements for a fiber positioner system and gives a rationale for each of them. Depending on the rationale, the requirements can be ordered into 3 types: Section 2.1 lists the requirements which are derived from the science objectives of the astrophysical survey. Section 2.2 lists the requirements which guarantee the efficiency of the instrument, mainly by preventing loss of light. Section 2.3 lists the requirements which are due to the working environment on the telescope. Figure 2.1 gives an overview of the dependencies between the rationales and the requirements.

The content of this section is based on a published paper: "High density fiber postitioner system for massive spectroscopic surveys", P. Hörler, L. Kronig, J.-P. Kneib, M. Bouri, H. Bleuler, and D. von Moos, *Monthly Notices of the Royal Astronomical Society* [26].

2.1   Science goals

Focal plane coverage

Any point in the focal plane should be reachable by at least one fiber (100% coverage). This is the minimum to be able to observe any target in the field of view of the telescope. Sky background subtraction using $\sim 10\%$ of the fibers may be insufficient because 1) the sky background can vary a lot across a wide field of view (particularly at infrared wavelength) and 2) most targets will be much fainter than the sky-background. We could increase the number of sky-fiber or in a more extreme case, we can arrange fibers in pairs: One fiber will be positioned on the target and the other one as close as possible next to it, thus allowing to measure
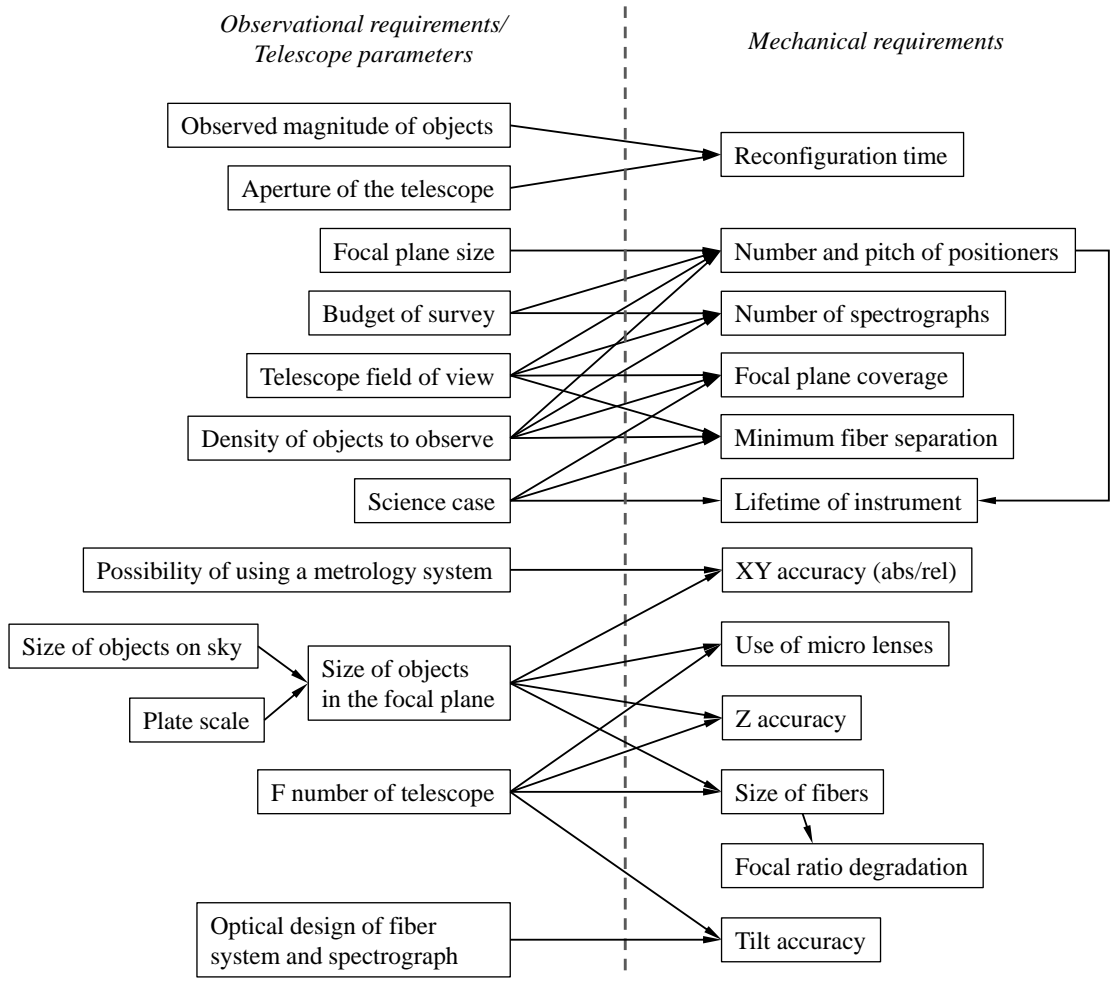
Figure 2.1: Overview on the dependencies between the rationales and the requirements of a robotic fiber positioning system.

the sky background close to the target. This means that any point in the focal plane has to be reachable by at least two fibers (a coverage of at least 200%).

The mechanical constraints of the positioner and particularly of the fiber holding part, should allow two fibers to be placed as close as possible to each other. If a machined part holding a ferrule is used, the minimum distance is typically a few millimeters in the focal plane (around one arc-minute on sky). For tilting spines the minimum distance can be shorter as the fiber tips are only surrounded by the thin spine.

In some cases, when the survey uses multiple spectrographs (for example a visible and an IR spectrograph), one fiber positioner could hold more than one fiber. If the spectrographs do not accept the same number of fibers, there will

be part of the positioners carrying both types of fibers and another part of the positioners carrying only one type of fiber. In that case a coverage of more than 200% is preferred as it will allow to cover nearly 100% of the focal surface using only half of the positioners.

Density of positioners / Pitch

The pitch between fiber positioners and therefore the spatial density of positioners is given by the focal surface area and the number of positioners. A rough relation between the pitch p, the focal surface area A_{foc} and the number of positioners N_{pos}, is given in equation 2.1:

$$p = \sqrt{\frac{2}{\sqrt{3}} \frac{A_{foc}}{N_{pos}}} \qquad N_{pos} = \frac{2}{\sqrt{3}} \frac{A_{foc}}{p^2} \qquad (2.1)$$

For an exact calculation of the number of positioners, some more details have to be taken into account: In addition to the fiber positioners, guide cameras/fiber bundles and metrology fiducials will have to be placed in the focal surface. One approach is to fill only a hexagonal shaped area within the circular focal surface, which leaves 6 wedges on the periphery for such devices. Figure 2.2 plots the number of positions (which can be filled by either a positioner or a fiducial) in function of the pitch for a circular focal surface of 800mm in diameter.

The focal surface area is a quantity defined by the existing telescope for which a new instrument is being designed. If a new telescope is to be built, or if an existing telescope can be modified (e.g. to allow a wider field of view), the focal surface should be maximized to facilitate the design of the fiber positioners. However, the ratio between the focal surface diameter and the field of view diameter of the telescope has to be designed such that the size of the observed objects match the size of the fiber pupils. For a given ratio, for example 100μm/arcsec, the focal surface area is proportional to the field of view of the telescope. A way to overcome this constraint is to add microlenses in front of each fiber as described in the next subsection.

The number of positioners on the other hand is mainly driven by the number of fibers the spectrograph can accept, which in turn is driven by the science case (usually the goal is to have as many as possible) and limited by the budget (the detectors of the spectrograph are generally the most expensive part of such an instrument).

Size of fiber cores

In most cases the fiber tips are located in the focal plane and an image of the observed objects is projected onto the fiber core. The fiber core acts as a field
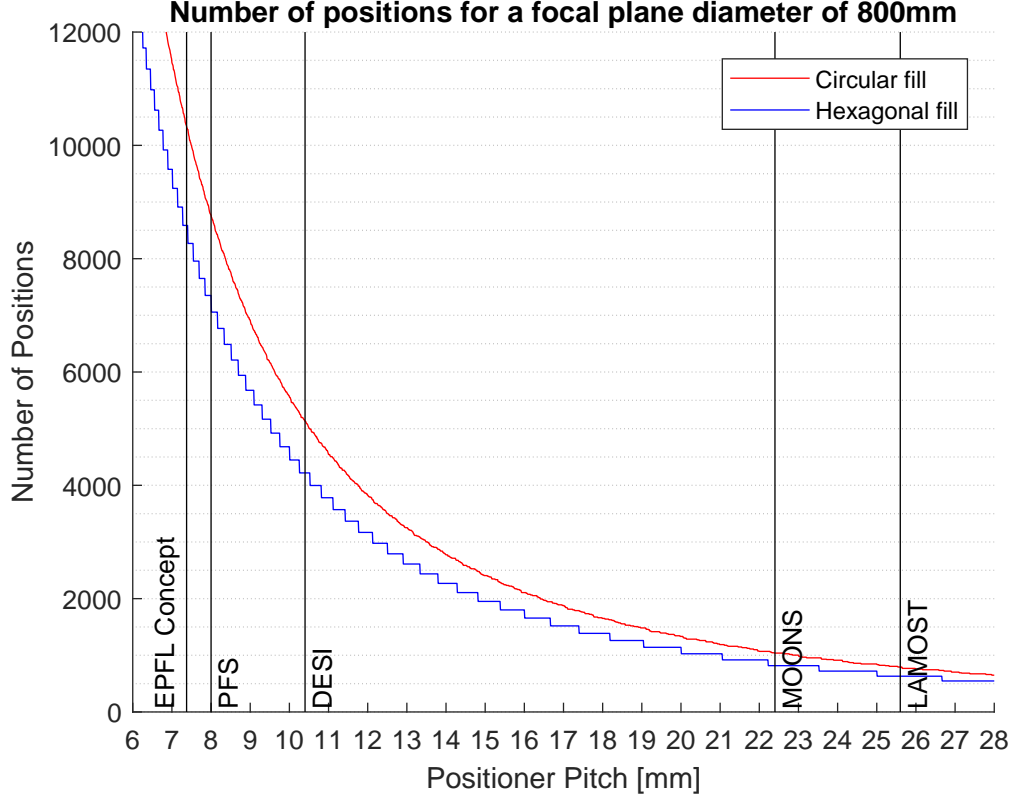
Figure 2.2: Number of positioners in function of the pitch. The red line is obtained filling the whole circular focal surface. The blue line is obtained filling only a hexagonal shaped area within the circular focal surface. The pitches of some projects are shown for reference.

stop and defines the light collecting area. Its size should match the typical size of objects (convoluted by the typical seeing size of the telescope site). Point objects and far galaxies are smaller than the typical seeing of 0.5" − 1" at most telescope sites. The typical plate scale of astronomical telescopes is $50 - 100 \mu m/arc-second$ so the fiber core size of a multimode fiber of $100 - 150 \mu m$ covers all objects.

In some cases the plate scale is bigger and a bare fiber would be too small. In that case one can add a microlens in front of each fiber. The microlens has to be placed in the focal plane and projects the light onto the smaller fiber core, changing the f-ratio. The cost is an increased complexity of the fiber assembly and an additional source of error (misalignment of the microlens with respect to the fiber) and throughput loss.

Another constraint on the fiber size is that the fiber should have a high transmission in the wavelength range of the objects to observe.

Stray light

Incident light of bright objects which are not observed can potentially be reflected by any surface on the positioners and end up in the fibers observing fainter objects. Therefore, any part of the positioners exposed to incident light should absorb as much light as possible to avoid stray light. This concerns all parts which are located between the focal plane and the support plate and are exposed to incident light. Their surfaces should be treated to maximize absorption (for example black anodizing) and if possible inclined with respect to the focal surface. It is also possible to add a light-trapping blind hole on the beta arm of a positioner. In this way the light of an extremely bright star can be trapped in the blind hole of one dedicated positioner.

Lifetime and reconfiguration time

The lifetime of the instrument is driven by the scientific goals of the survey, for example 10^6 measurements over 10 years. The available time on the telescope should be used efficiently for exposures and the time between two exposures has to be kept as short as possible. The time between two exposures is used to readout the detectors, slew the telescope and reconfigure the fibers for a new field. The reconfiguration time of the fiber positioners should not be longer than the readout and slew time, typically in the order of 60 seconds.

The usage of the positioners is very sporadic. The positioners are only moved during reconfiguration between two exposures. In order to ensure such lifetime given the usage, the actuators have to be designed with suitable characteristics regarding lubrication and preload.

2.2 Instrument efficiency

This subsection lists all requirements which aim to reduce loss of light between the telescope and the spectrograph.

XY accuracy

A positioning error of the fiber in the XY plane induces loss of light by vignetting. On one hand some of the light of the object will not fall onto the fiber, and on the other hand more sky background will be collected. The tolerance on the XY positioning error is therefore proportional to the fiber core diameter. Small, seeing-limited objects (figure 2.3 bottom) have a projected image about the size of the fiber core and a XY Error of a few percent of the core diameter is acceptable. Typically the XY tolerance is $\sim 4\%$ of the core diameter ($\sim 5\mu$m for a 125μm

fiber core in DESI and $\sim 20\mu$m for a 600μm microlens in MOONS). For closer and larger objects (figure 2.3 top), for which the projected image is larger than the fiber core, the throughput loss depends on the intensity profile, but is smaller and a larger tolerance is generally acceptable.
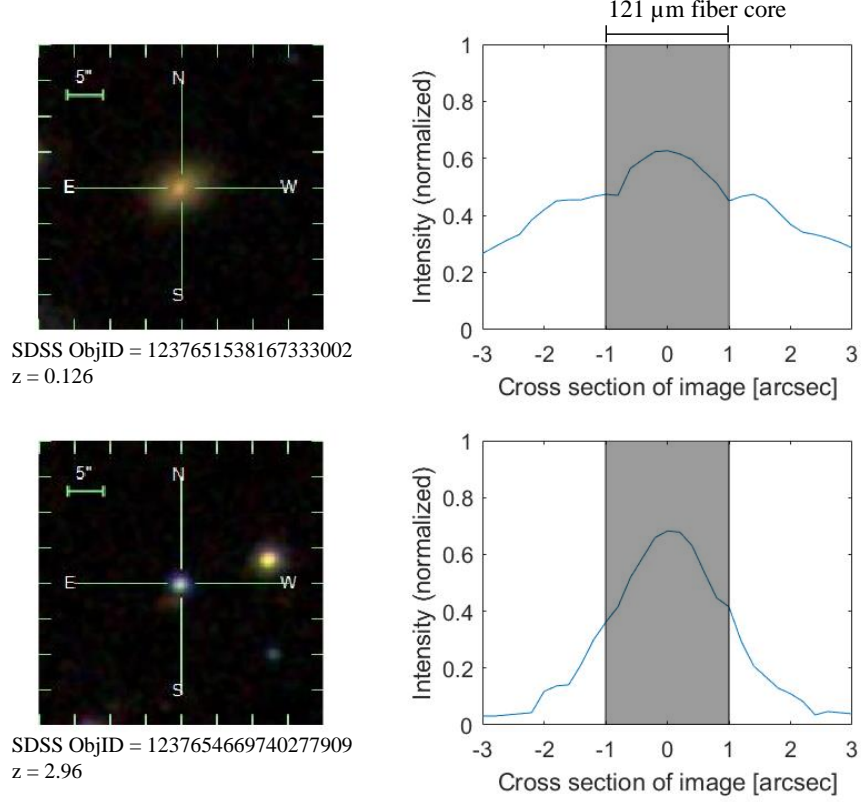
Figure 2.3: Comparison of target and object size. The images and fiber size are taken from the SDSS survey. Image source: http://skyserver.sdss.org

Z accuracy

An error in the Z-direction moves the fiber out of focus which will result again in light loss as the projected image of the object gets larger than the fiber pupil as can be seen in figure 2.4. The relative increase of the diameter d depends on the error in the Z-direction Δz, the f number of the light f and the diameter itself:

$$\frac{\Delta d}{d} = \frac{\Delta z}{df} \tag{2.2}$$

The exact amount of light loss however depends on the brightness distribution across the object itself. A typical Z tolerance for a 125μm fiber and a f number of 4 is $\sim 50\mu$m.
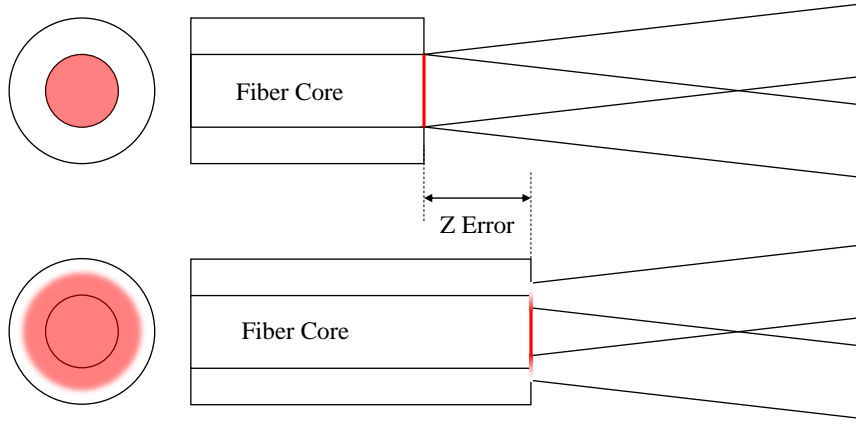
Figure 2.4: Illustration of the effect of a Z error (out of focus error).

Tilt accuracy

The fiber tip (and microlens assembly if applicable) has to be aligned with the chief ray, perpendicular to the focal surface. Any tilt error will induce focal ratio degradation in the fiber which will finally cause throughput loss. The requirement for the tilt error depends on the f number of the telescope, the fiber and how the spectrograph is designed. Usually the acceptance angle of the fiber is slightly bigger than the light cone coming from the telescope and the collimator in the spectrograph accepts a fiber output beam a bit faster than the nominal one. Both of these measures increase the acceptable tilt error. A tilt error is effectively decreasing the f number of the incident light. A tilt error of 0.2° on a $f/4$ beam will decrease the f number to 3.89. In these cases the tolerance on the tilt of the fiber is typically a few tens of degrees.

In some cases however, the f number of the telescope is smaller than the one accepted by the fiber. For example the primary focus of the Subaru telescope is $f/2$. In these cases the fiber has a bigger f number and acts as an aperture stop. A tilt error has no effect until the light cone accepted by the fiber exits the light cone coming from the telescope. For example a fiber accepting a $f/3.6$ beam on a $f/2$ telescope, can have a tilt error of up to 6.1° without throughput loss.

FRD due to fiber stress

Another source of light loss lies within the fiber. Mechanical stress degrades the focal ratio in the fiber. The fiber path has to be chosen in a way to minimize stress in the fiber. In general we can say that bending and contact with sharp edges has to be avoided. However, it is not obvious to define a requirement on fiber stress for the mechanical design. A solution is to define a minimum bending radius of the fiber (for example 50mm) which can be estimated using Ramseys formula [36] or has to be determined experimentally on test fibers.

$$\frac{\Delta\Theta}{\Theta} = \frac{d}{R} \tag{2.3}$$

Θ is the angle of the incident light with respect to the fiber axis, $\Delta\Theta$ is the radial dispersion, d is the core diameter and R is the bending radius. An illustration is shown in figure 2.5.

Torsional stress has also to be considered, especially in the case of the $\alpha - \beta$ geometry (SCARA-like). In such designs, the fiber should not be constrained on the positioner, such that a rotation of the fiber tip is distributed over a bigger length, ideally until they are bundled. In that case FRD due to torsion can be constrained. Again, this has to be verified experimentally, especially for large fiber diameters.

Another solution is to define a maximum throughput loss due to fiber stress (for example 0.5%). This number can only be verified on a prototype positioner with a test fiber, whereas a minimum bending radius can be taken into account during the design phase of the positioner.

The spectrograph design usually has a built in tolerance for FRD by accepting a slightly faster beam than the nominal one. The tolerance on the FRD of the fiber depends therefore also on the spectrograph design.

Difference in focal ratio between fiber input and output

Except for the FRD described above, the focal ratio at the output of the fiber is equal to the focal ratio at the input of the fiber. In order to maximize the throughput of the fiber, the input and output focal ratio should correspond to the nominal numerical aperture (NA) of the fiber. The focal ratio of the telescope can be corrected for the fibers using a field corrector (one for the whole field) or microlenses (one per fiber), both of which introduce additional throughput loss due to absorption and misalignments. If a new telescope is being designed, the focal ratio of the telescope should be designed to match the NA of the fibers.

In the example of the DESI instrument, the telescope projects light at f/4 and the spectrograph can accept light at f/3.57.
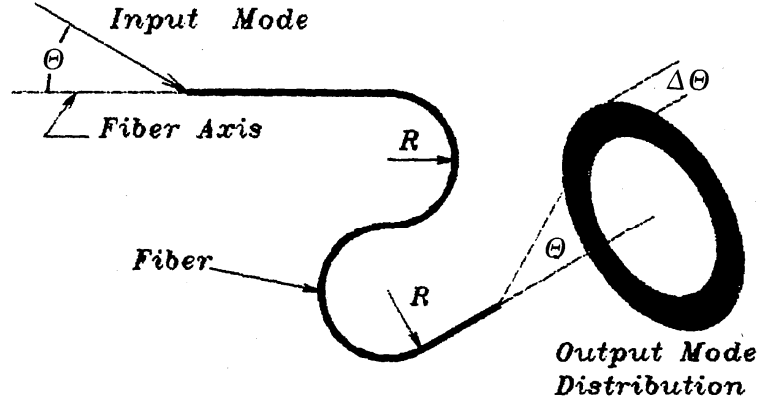
Figure 2.5: Illustration of FRD. Source: [36]

In the example of the MOONS instrument, the focal ratio of the telescope and field corrector is f/15. The focal ratio at the output of the fibers in the spectrograph is f/3.5. The microlenses project the light at f/3.65 onto the fiber core. In this way, the transmission loss due to the focal ratio difference is less than 2.5%.

2.3   Environmental constraints

Operational temperature and humidity

As the fiber positioners are placed in the focal plane of the telescope, they are typically located in the dome of the telescope. This means that the operating temperature has to be kept within few degrees Celsius of the ambient night temperature in the dome. In the case of the Mayall (DESI), VLT (MOONS) and Apache Point (SLOAN) this temperature varies between $-10°$C and $30°$C.

Similarly, for good transparency of the atmosphere, the humidity has to be very low at the site of the telescope. These factors are to be taken into account in the mechanical design when choosing the lubricant of the ball bearings and the gearbox and glue, if any.

Heat dissipation

The *average* power consumption of the positioners is limited by thermal considerations: If the positioner dissipates too much heat toward the focal plate and the environment, thermal expansion will introduce XY errors to the fibers and worse, create turbulences in the dome and disturb the seeing of the telescope. As the positioner is idling the majority of the time, the actuators are not powered while

25

idling and the local drive electronics is turned off or put into low power sleep mode. In that way, the average heat dissipation can be kept low. *This means that the positioners have to keep the position of the fibers passively during the observations.* In the case of motors and gearheads, this is an argument in favor of irreversible gearheads which makes them hold the position passively.

The *maximum* power consumption in the active state is mainly limited by the electrical current supply to the focal plate. In the case of the DESI instrument, each positioner typically consumes several hundred mA at 5 to 10V. If we consider 5000 positioners, the whole focal plate needs over 1kA at 5 to 10V. The high current requires a special power supply and bulky, heavy electrical connections between the power supply and the focal plate.

Earthquake resistance

In the case of the VLT, the telescope is located in an earthquake active area. There is a very high probability that an instrument will have to resist a strong earthquake within its lifetime. Therefore the mass of the positioner is critical for the structural integrity of the instrument. In the case of the MOONS instrument, structural simulations suggest a limit of 200g per positioner.

Collision avoidance

The possibility for pairwise observation of targets (one fiber on the target and one next to it for background subtraction) requires overlapping workspaces, which creates a risk for collisions between adjacent positioners. A decentralized path generation algorithm is necessary to guarantee collision-free trajectories for all positioners in a practical amount of time [31].

2.4   Summary

A summary of the different requirements and their rationale as well as a numerical example taken from the MOONS instrument is presented in table 2.1.

Rationale	Requirement	Example value
Pairwise observation	Focal plane coverage	Each position reachable by at least 2 positioners
Pairwise observation	Minimal fiber distance	4mm
Telescope field of view and science goal	Pitch	25mm
Target size	Size of the pupil	$610\mu m$
Survey length	Lifetime	10^6 Movements / 10 years
Science goal	Reconfiguration time	< 30 sec
Instrument efficiency	RMS XY Error	$< 20\mu m$
Instrument efficiency	Z max defocus error	$< 50\mu m$
Instrument efficiency	Max tilt error	$\pm 0.15°$
Instrument efficiency	FRD due to fiber stress	$< 0.5\%$ throughput loss
Instrument efficiency	Difference in focal ratio between fiber input and output	$< 1\%$
Environment temperature	Operational temperature	$-10°C$ to $+30°C$
Environment humidity	Operational humidity	5% to 20%
Low heat dissipation	Power while active	$< 2W$
Low heat dissipation	Power while inactive	0W
Earthquake resistance	Mass of the positioner	$< 200g$

Table 2.1: Example of Fiber positioning requirements.

Chapter 3

Existing technologies: a comparative perspective

There are mainly three alternative technologies that can be used for MOS: slit masks, micro mirror arrays (MMA) and fiber positioning. In the following section, the first two technologies are presented and an explanation why fiber positioning is better adapted for massive MOS is given. Then, an overview of currently existing fiber positioning solutions is presented.

3.1 Slit masks and micro mirror arrays

The principle of a slit mask is to cover the image of the sky and let pass only the light of target objects at specific locations. After the slit mask, a grating or prism will split up the light according to wavelength and a detector can then read spectral lines. As the spectral lines are located according to the location of the objects in the field, they can potentially overlap, and the detector real estate is not used efficiently. An example is the IMACS instrument which uses laser-cut aluminium plates as slit masks [11]. It can handle up to around 400 objects in parallel. A more advanced instrument is MOSFIRE, which has a reconfigurable slit mask mechanism [45], but can handle only 46 objects in parallel.

A micro mirror array works in a similar way, but instead of *transmitting* it *reflects* the light of the target objects towards a spectrograph as shown in the right part of figure 3.1. The micro mirrors can typically be tilted in two stable positions: On and Off, where the On mirrors reflect light towards the spectrograph, and Off mirrors towards a light trap. In more advanced instruments like RITMOS [32] or SAMOS [37], there is an imaging system instead of the light trap. In this way, the brightest objects can be used for spectroscopy, while the darker rest of the field can be imaged without the glare of the bright objects at the same time.

29
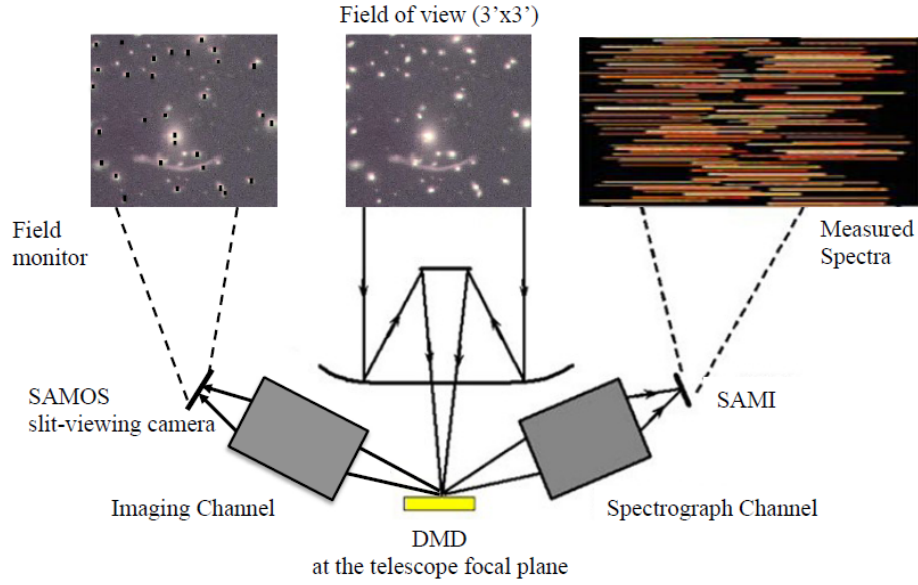
Figure 3.1: Principle of using a micro mirror array for multi object spectroscopy (DMD stand for digital micromirror device). Image source: [37] (The SAMOS and SAMI acronyms seem to be inverted in this figure)

When using micro mirror arrays, the spectral lines are located according to the location of the objects in the filed. This means that they can overlap, and the detector real estate is not used efficiently. These devices are however extremely fast compared to other technologies. If a transient object is detected on the imaging side, the corresponding mirrors can immediately switch to the spectroscopy side. Another advantage is that they are relatively simple and lightweight in comparison to a fiber positioning system which makes them good candidates for space telescopes.

3.2 Fiber positioning

In a fiber positioning solution, multiple optical fibers are used to transmit the light of target objects to a spectrograph. One end of the fibers has to be placed on the objects in the focal plane, while the other ends are arranged in the slit of the spectrograph. In this way, the location of the fibers is not constrained in the focal plane, and the detector real estate is used very efficiently as all spectral lines are aligned next to each other.

Different mechanical solution for the positioning of the fibers have been developed and realized in the past and present. They can be categorized in 3 categories: 1) manual placement in previously drilled holes in a metal plate 2) Robotic

pick-and-place of magnetic fiber buttons on a metal focal plate 3) Robotic fiber positioners in the focal plane. They are described in the following sections.

- manual placement in drilled holes in focal plate

- Robotic pick-and-place on magnetic focal plate

- Robotic positioners

    - $\alpha - \beta$ robotic positioners
    - $R - \Theta$ robotic positioners
    - Tilting spine positioners
    - Starbugs

Table 3.1 summarizes MOS surveys which use movable fibers in combination with a spectrograph. The key properties which are given are the technology used for fiber positioning, the telescope mirror diameter, the field of view of the telescope, the number of fibers, the pitch of the positioners (if applicable), the patrol area diameter (if applicable), the precision of positioning, the plate scale, the minimum fiber separation, the reconfiguration time and the the year of the instrument availability.

Instrument	Telescope	Technology	Mirror ⌀m	FOV ⌀deg	Nb. of fibers	Pitch mm	Patrol area ⌀mm	Precision μm	Precision arcsec	Plate scale μm/arcsec	Minimum fiber separation mm	Minimum fiber separation arcsec	Time to target sec	Year
2dF	AAT	Magnetic fiberbutton	3.9	2	400			20	0.3	66.7	2	30	2400	1996
APOGEE 1&2	Sloan	Manual plugging	2.5	3	300			25	0.35	60.6			3600	2000
BOSS/eBOSS	Sloan	Manual plugging	2.5	3	1000			25	0.35	60.6			3600	2000
FLAMES	VLT	Magnetic fiberbutton	8.2	0.417	130			58.8	0.1	588	6	10.2	900	2003
Hectospec	MMT	Magnetic fiberbutton	6.5	1	300			25	0.15	166.7	3.4	20.4	300	2004
Hydra	WIYN	Magnetic fiberbutton	3.5	1	90			30	0.3	106.7	3.95	37	1200	2005
FMOS	Subaru	Tilting spine	8.2	0.5	400	7.2	14.5	10	0.1	83.3	1	12	780	2012
LAMOST	LAMOST	Alpha-Beta	4	5	4000	25.6	33	40	0.4	100			600	2012
TAIPAN	UK Schmidt	Starbugs	1.2	6	150	17		4.55	0.3	15.1	9	594	300	2016
MOHAWK	Blanco	Tilting spine	4	2.25	4000	6.75	16.2	10	0.18	55.5	0.5	9	15	2016
PFS	Subaru	Alpha-Beta	8.2	1.3	2400	8	9.5	5	0.054	92.6	3	32.4	40	2017
MANIFEST	Giant Magellan	Starbugs	24.5	0.33	2000	6.3	20	20	0.02	1000	8	8		2017
DESI	Mayall	Alpha-Beta	4	3.2	5000	10.4	12	5	0.07	71.4	2	28	45	2018
WEAVE	WHT	Magnetic fiberbutton	4.2	2	1000			11.22	0.2	56.1	3.4	60.60	3600	2018
MEGARA	GTC	Alpha-Beta	10.4	0.066	100	20.1	23.21	25	0.15	166.7			10	2018
4MOST	VISTA	Tilting spine	3.7	2.5	2400	8.8	21	10	0.17	58.8	1	17	60	2019
MOONS	VLT	Alpha-Beta	8.2	0.417	1000	25	50	20	0.035	578.3	5	8.67	15	2019
SDSS-V	Sloan	Alpha-Beta	2.5	2.87	500	22.4	44.8	9.7	0.16	60.6	5	82.5	120	2020
SDSS-V	du Pont	Alpha-Beta	2.5	1.9	500	22.4	44.8	10.09	0.11	91.7	5	54.5	120	2020
MSE	*CFHT*	*Tilting spine*	*10*	*1.5*	*4332*	*7.77*	*19.27*	*6*	*0.056*	*107*	*0.75*	*7*	*6*	*2021*

Table 3.1: This table summarizes existing Fiber positioning systems. The MSE instrument is in an early stage of development, so the parameters are subject to change.

3.2.1 Manual placement in drilled holes in focal plate

This technique does not use robotic positioners. The fibers are manually inserted into holes of an aluminium plate which are drilled at the desired positions. This method is very simple and presents a low risk, but requires a large amount of plates and manual work: For each exposure, a new plate has to be manufactured and populated with fibers. As the targets have to be defined long before the exposure, this technique makes it impossible to adapt for transient objects with a short notice. Just the exchange of already populated plates on the telescope takes around 1 hour, which is lost observation time on the telescope.

This technique is used in the Sloan Digital Sky Survey I - IV (SDSS I - IV) on the Sloan foundation telescope [13, 7].
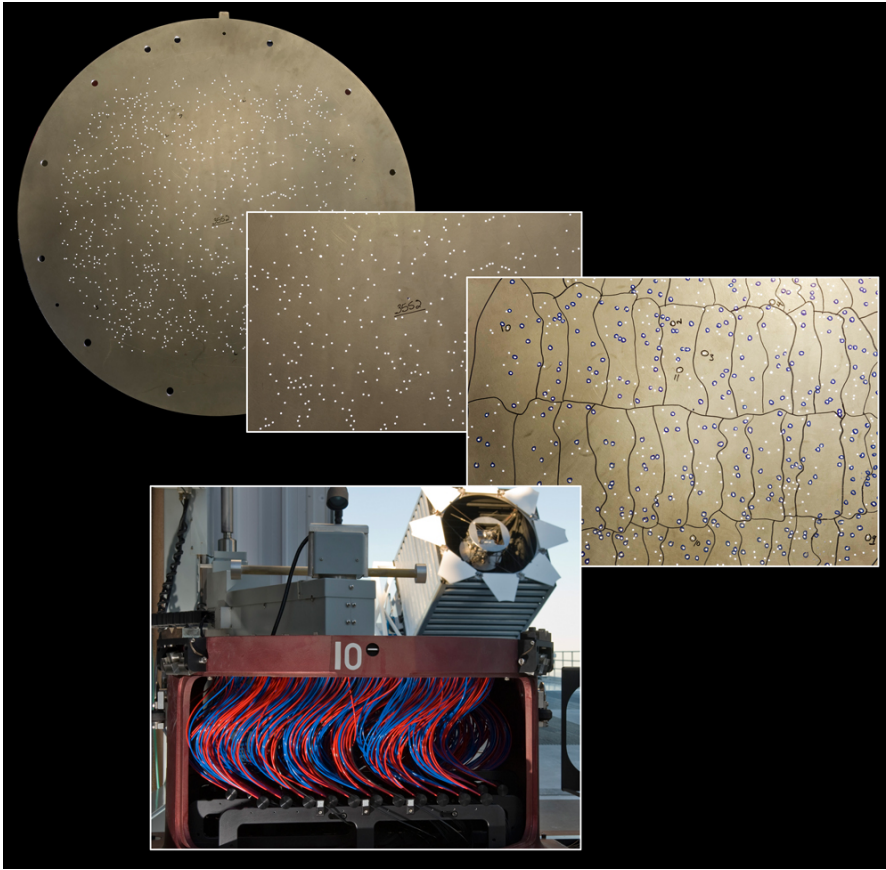
Figure 3.2: Top: Aluminium plate with drilled holes to define the target locations. Bottom: Fibers plugged into a plate on the way to be installed on the telescope. Source: http://newscenter.lbl.gov/2012/08/08/boss-sdss-dr9/ Credit: Lawrence Berkeley National Laboratory, Apache Point Observatory and the SDSS-III Collaboration.

3.2.2 Robotic pick-and-place on magnetic focal plate

In this method the focal plane is a flat metallic surface where magnetic fiber buttons can be placed. The fiber buttons are parked in the circumference of the plate and are then picked and placed to their targets by one or several robotic arms. The drawback of this method is that the reconfiguration process is serial and takes typically tens of minutes to one hour. Target assignment and its optimization is also very complex, because each fiber can only access a certain part of the focal plane, collisions between fiber buttons have to be avoided and fiber crossings limited. This method is used in in the AAOmega + 2dF [25], Hectospec [14], Hydra [5, 4], FLAMES and WEAVE [29] instrument.
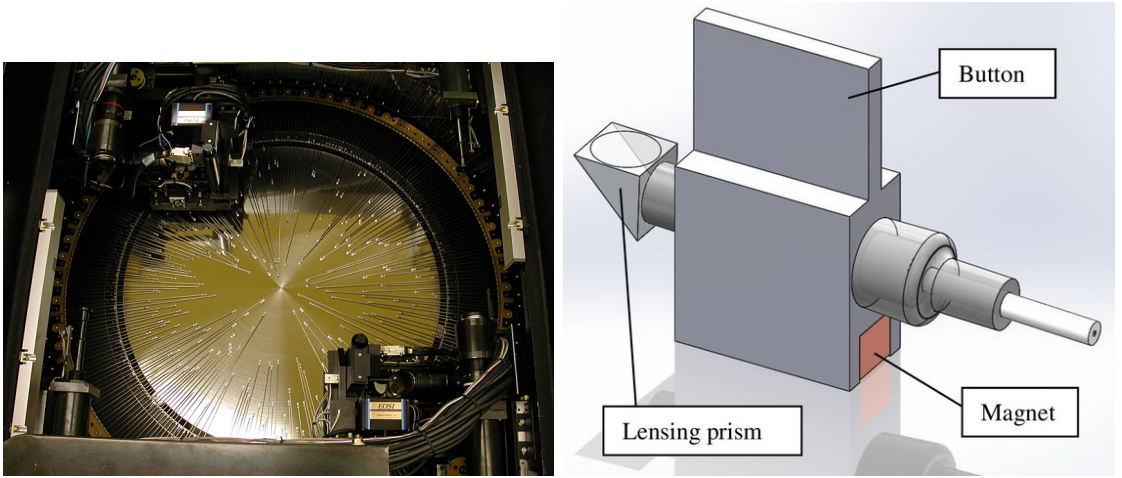
Figure 3.3: *Left*: View on the focal plane of the Hectospec instrument. In the top left and bottom right the two pick-and-place robotic arms are visible [14]. *Right*: Concept of one fiber button of the WEAVE instrument [41].

3.2.3 Robotic positioners

This section summarizes different robotic fiber positioners where one positioner per fiber or IFU is used. Each positioner holds a fiber or IFU and is able to place it in a local workspace which covers a small portion of the focal plate. As the workspace of a single positioner is in general circular, the workspaces of neighboring positioners have to overlap. Otherwise, some part of the focal plane would remain unreachable. The general advantage of this technology is that the fibers are reconfigured in parallel and very short reconfiguration times can be achieved. The challenges are the miniaturization needed to achieve the density of positioners. And collision avoidance.

Tilting spine positioners

In this technology the fiber is guided in a spine which pivots around a sphere at the base of the positioner. The rotative stick and slip movement of the sphere is generated by a piezo tube attached to the sphere. The tilting of the spine creates a displacement of the fiber tip in the focal plane which is used to place the fiber to its target location. The advantages of this method are that the fiber flexure is very small and the mechanical design is very simple. The disadvantage is that the repeatability of the stick and slip motion is of about 10% of the travel distance. This means that there must be a metrology camera to measure the error and iterate which leads to long reconfiguration times of typically several minutes. Another disadvantage is that the spherical motion of the fiber tip induces a tilt and Z (out of the focal plane) error. It is used with 400 fibers on the FMOS instrument [21, 1, 33, 22] and planned with 2400 fibers on the 4MOST instrument [8]. A concept with 4000 fibers called MOHAWK was studied for the Subaru telescope [39, 38], but was discarded in favor of the Cobra $\alpha - \beta$ positioner as part of the PFS instrument.
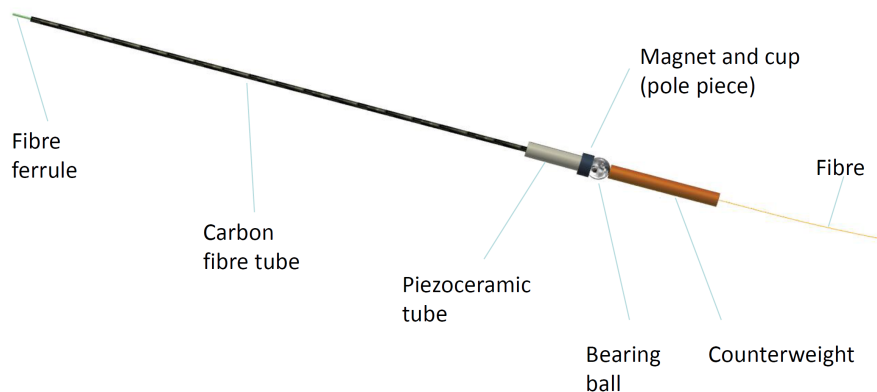
Figure 3.4: Principle of the tilting spine positioner. Example of the MOHAWK positioner [39].

Starbugs

The Starbugs are mobile positioners where the positioner itself moves to the target of the fiber. The positioners are mounted under a transparent focal plate and can move freely in the whole focal plane. The actuators are two piezo tubes which produce a stick and slip motion. Because of the low repeatability of the stick and slip motion, positioning iterations have to be made using a metrology camera. Special attention has to be given to the target assignment and the positioner

35

trajectories to avoid fibers warping around each other. The disadvantage of this technology is that the fiber density in the focal plane is much lower than with fixed positioners. This method will be used by the MANIFEST instrument [23, 20].
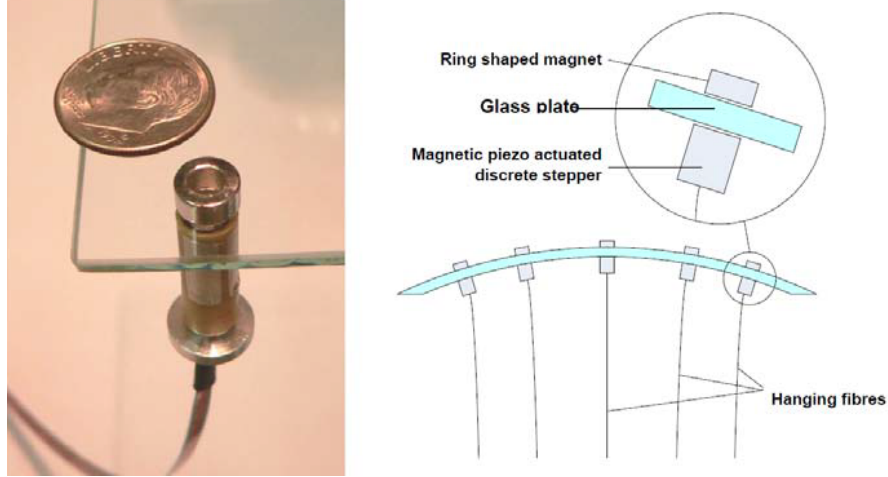
Figure 3.5: Starbugs - mobile positioners under a transparent focal plate [24].

$\alpha - \beta$ robotic positioners

This concept is based on a two arm serial robot with two parallel rotational joints, α and β, similar to the SCARA kinematics. The α axis is in the centre of the positioner and the β axis is eccentric. In this way the fiber moves in a planar motion and is not tilted. The resulting workspace has an annular shape as shown in figure 4.1. If both arms have the same length, the workspace is a circle centred on the positioner.

The actuators are electric motors of different types. Stepper motors are used in the LAMOST [19, 48] and MOONS [6] positioners. Brushless motors are used in the DESI [15, 43] positioners. Piezo motors are use in the PFS [17, 16] positioners. The transmission of the movement is also of various types. Direct drive is only used in combination with piezo motors in the PFS positioners. The brushless and stepper based positioners use a reduction gearbox with a high reduction rate in order to achieve a resolution high enough to meet the precision specification. In the MOONS and DESI positioners the motors and gearboxes are mounted on the axis of the output. In the LAMOST and the Swiss-Spanish positioner for DESI (shown in figure 3.6) the motors and gearboxes are mounted off axis and additional gears are used to transmit the motion to the output. An advantage of the $\alpha - \beta$ design over others is that it allows for a short reconfiguration time of less than a minute.

36

A decentralized path generation algorithm may be necessary to guarantee collision-free trajectories for all positioners in a practical amount of time [31].
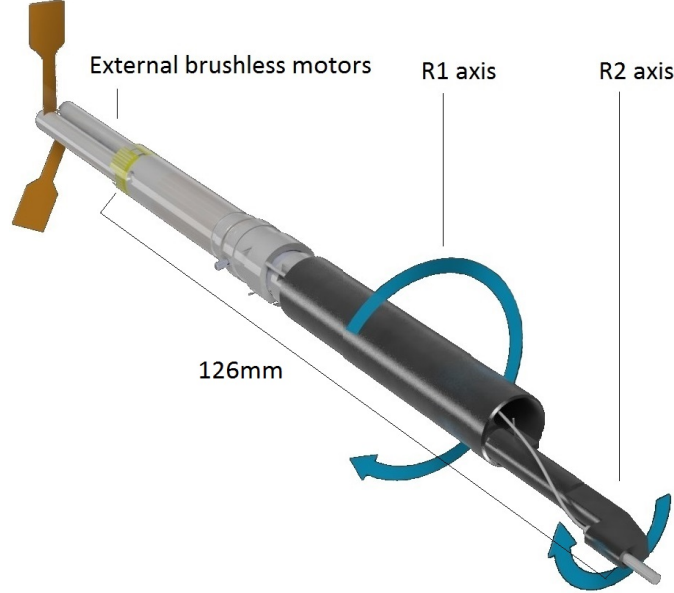
Figure 3.6: $\alpha - \beta$ positioner designed by AVS. R1 is the α axis and R2 is the β axis. [15].

$R - \Theta$ robotic positioners

This concept is similar to the $\alpha - \beta$ design, but the β rotation is replaced with a radial translation R. Similarly, the resulting workspace is a circular disk. The main advantage is that being able to move radially, the collision avoidance strategy becomes easier and potentially the target-assignment efficiency can be increased. The challenge with this concept is the realisation of the radial movement within the mechanical envelope of the positioner. Two concepts have been studied, but none have been used in a telescope: One for the DESI project in 2012 [44], and one for the 4MOST instrument in 2014 [40].

3.3 Summary

Tables 3.2 and 3.3 give a summary of the advantages and disadvantages of the different technologies.
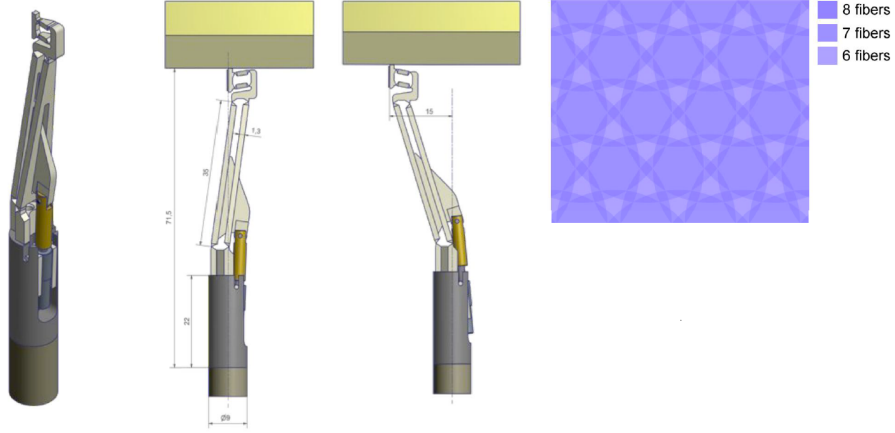
Figure 3.7: $R - \Theta$ positioner concept for the 4MOST instrument [40] which was rejected in favor of a tilting spine solution.

Technology	Number of Targets	Reconfiguration speed	Cost and complexity
Slit mask	- -	- -	+
Micro mirror arrays	-	++	+
Manual fiber plugging	+	- -	-
Robotic pick-and-place	+	-	-
Robotic positioners	++	+	-

Table 3.2: Comparison between different technologies for MOS

Technology	Advantages	Disadvantages
Tilting spines	High fiber density Good Coverage Cost effective	High tilt and out-of-focus errors Relies on a metrology system
$\alpha-\beta$ positioners	High fiber density Low tilt and out-of-focus errors Can work without metrology Medium Coverage	High cost and complexity
Starbugs	Good for clustered targets Low tilt and out-of-focus errors	Low fiber density Relies on a metrology system

Table 3.3: Comparison between different fiber positioners. The $R-\Theta$ positioner is not listed as it has the same advantages and disadvantages as the $\alpha - \beta$ positioner but has never been implemented on an instrument.

Chapter 4

Positioner design guidelines and technological limitations

This chapter aims to give design guidelines to choose a geometry and define the design parameters for a given survey and telescope in section 4.1. It furthermore shows the limits of fiber positioning technologies in section 4.2.

4.1 Design guidelines for high precision and accuracy

This section is organized in 2 parts: First, the different geometries of fiber positioners from section 3.2.3 are compared in terms of focal plane coverage in section 4.1.1. Second, section 4.1.2 discusses detailed design elements of a $\alpha-\beta$ positioner.

4.1.1 Focal plane coverage and positioner geometry

The coverage of the focal plane is an important parameter of a fiber positioning system. It defines how many fibers can be placed on a given location in the focal plane. A minimum of 100% coverage, which means that any point in the focal plane is reachable by at least one fiber, is usually a minimum requirement. A double coverage of 200% or more can be required for pairwise observation modes. The coverage is defined by the geometry and pitch of the fiber positioner. For the $\alpha-\beta$, the $R-\Theta$ and the tilting spine geometries, the workspace of one positioner is circular and can have a circular hole in its center if the positioner cannot reach its own center. A small overlap of workspaces is therefore necessary to reach a 100% coverage. By increasing the overlap of the workspaces, the coverage is increased but the collision avoidance strategy becomes more complex.

As long as the own center can be reached, the radius of the workspace is a trade-off between coverage and mechanical/collision avoidance complexity. If however the own center cannot be reached, the outer radius of the workspace has to be at least as large as the pitch such that the centers of the adjacent positioners can be reached.

The following lines describe the focal plane coverage for the 4 geometries introduced in section 3.2.3.

- $\alpha - \beta$

  We can distinguish two approaches:

  - *Single coverage*: In this approach, both arms of the positioner have the same length, allowing it to reach its own center. The workspaces are full circles which overlap just enough to cover the whole surface. Thus, most of the surface is covered by a single fiber as shown in figure 4.2 (top left).

  - *Double coverage*: In this approach, the second arm is longer than the first arm. The positioner cannot reach its own center and the circular workspace has a hole in the center as shown in figure 4.1. To cover the whole focal surface, the arms have to be long enough to reach the center of the adjacent positioners. The resulting overlap guarantees at least a double coverage of the whole plane as shown in figure 4.2 (top right).

  In the case of the double coverage, the exact ratio between the arm lengths has to be chosen. For a maximum coverage we want to minimize the ratio i.e. minimize the hole in the workspace. Figure 4.3 (top) shows the effect of the arm-length ratio on the focal place coverage. The limit is given by the condition of no mechanical collision between positioners: If the alpha arm is too long, it will collide with the alpha arm of the adjacent positioner. The maximum length of the alpha arm l_α is given in function of the pitch p and the diameter of the guidance and actuator of the beta axis d_β:

  $$l_\alpha \leq \frac{p}{2} - d_\beta \tag{4.1}$$

  Figure 4.3 (bottom) shows the average coverage and the maximum guidance and actuator diameter d_β in function of the arm ratio. We can see that with smaller actuators, we can get a smaller arm ratio and a larger average coverage.

- $R - \Theta$
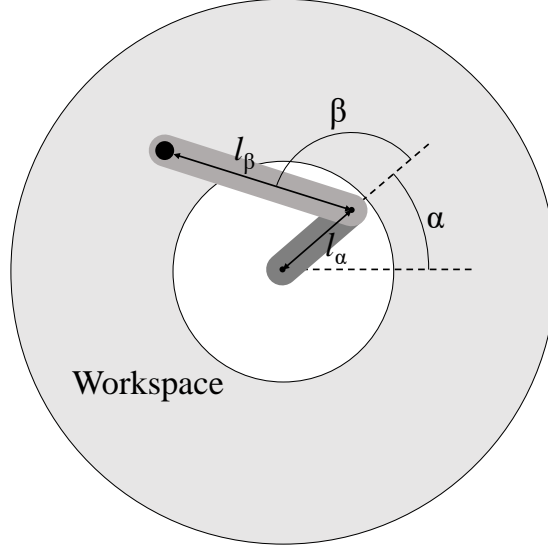
Figure 4.1: Kinematics and workspace of an $\alpha - \beta$ positioner using the double coverage approach.

With the $R - \Theta$ geometry, there are the same two approaches: Either the positioner can cover its own center or it can reach to the center of an adjacent positioner. Once the approach is chosen, the goal is to maximize the radial range. The coverage will look like the one of the $\alpha - \beta$ geometry shown in figure 4.2.

- Tilting spines

  A tilting spine can always reach its own centre. The goal is to maximize the radial range in order to maximize the coverage. With tilting spines it is common to achieve a radial range larger than the pitch of the positioners. The radius of the workspace will be a trade-off between the coverage and the allowable tilt error as the tilt error increases with radius. An example of such a coverage is shown in figure 4.2 (bottom). In this particular case the corresponding average coverage is about 520%.

- Starbugs

  In the starbugs case, every fiber can reach the whole focal plane, and the coverage is maximized. However, the minimum fiber separation is bigger, which makes pairwise observation modes difficult. The fiber density is further reduced, because the starbugs need some free space to be able to move.

**Nb. of fibers
reaching area**
1: yellow
2: green
3: red
4: light blue
5: purple
6: dark blue
7: orange
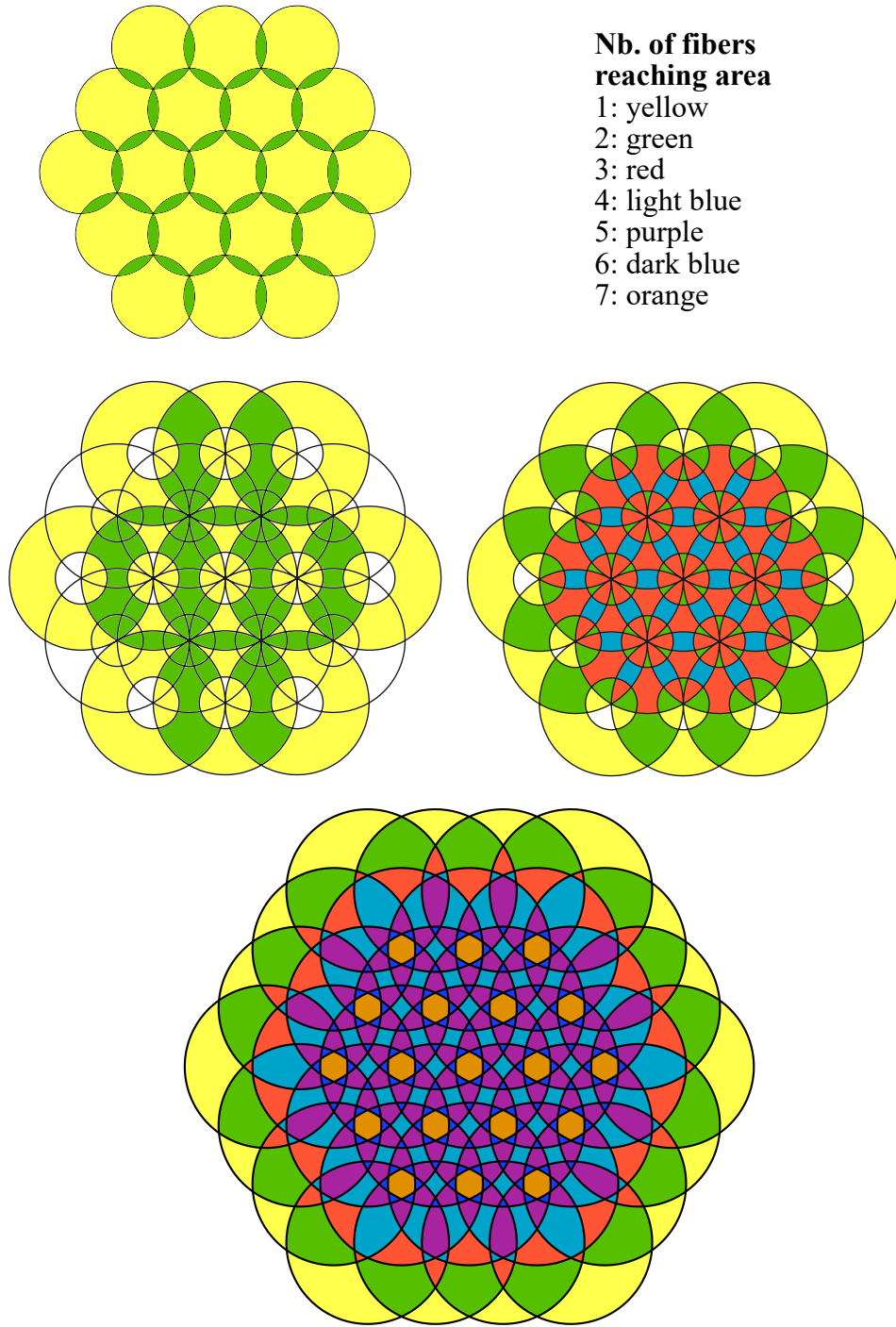
Figure 4.2: Focal plane coverage comparison between the $\alpha - \beta$ geometry single coverage (top left), double coverage (middle) and tilting spine geometry (bottom). Middle left shows the coverage using the double coverage geometry, but using only half of the positioners.
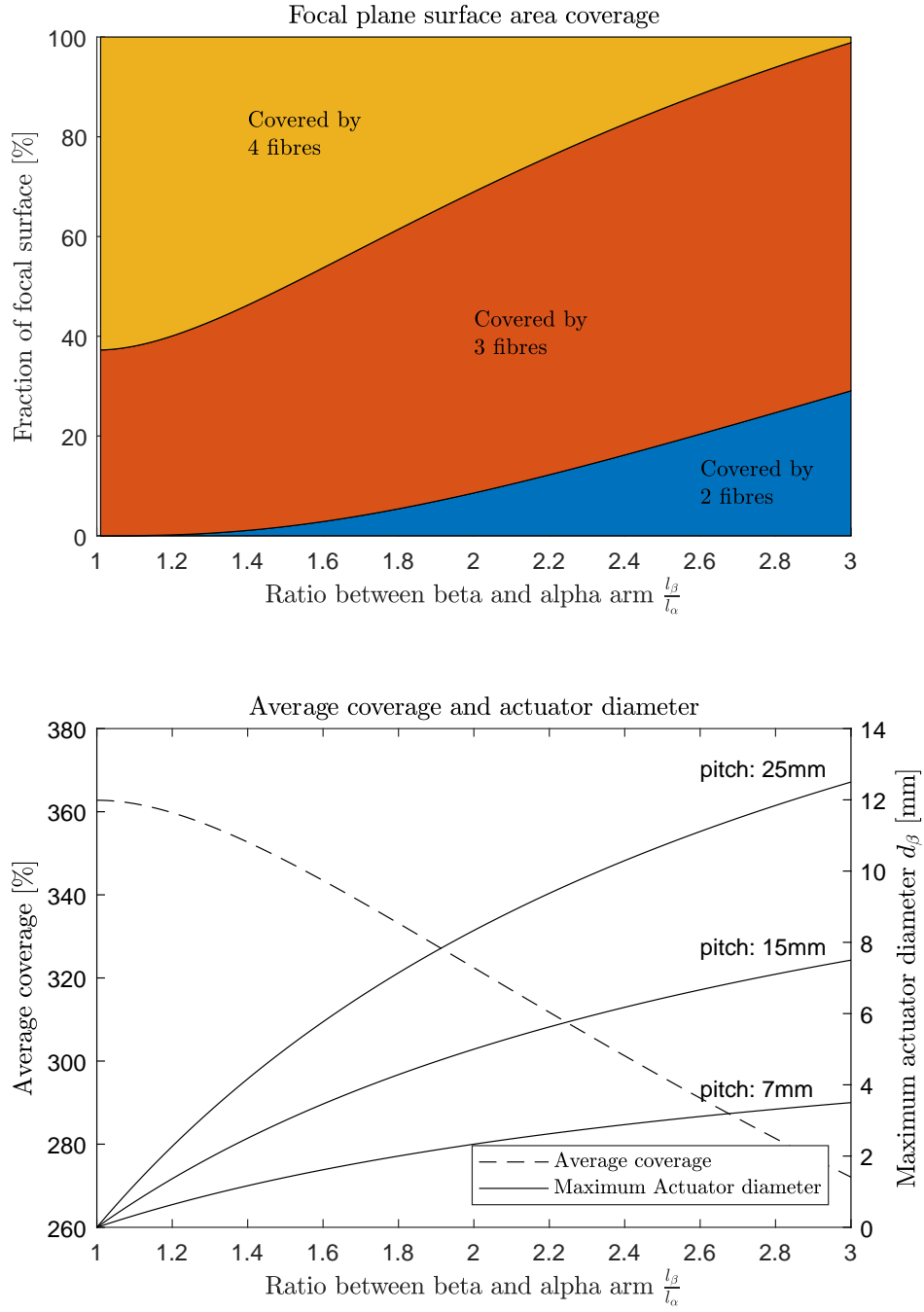
Figure 4.3: Focal plane coverage for the double coverage case in function of the arm length ratio. One can see that a smaller ratio gives a better overall coverage, but requires smaller actuators.

Cross-arm geometry: a theoretical concept

A new cinematic for a fiber positioner is presented in figure 4.4. The goal is to increase the focal plane coverage with respect to the dual-arm $\alpha - \beta$ geometry. It allows for a double coverage, while still being able to reach the own center, i.e. not having a whole in the workspace. This is interesting for instruments like the Maunakea Spectroscopic Explorer (MSE), which plans to cover the whole focal plane with only one third of the positioners.

The α pivot joint is the same as in the $\alpha - \beta$ geometry ((a) in figure 4.4), while the β pivot joint is replaced by 4 pivot joints (b,c,d,e) and two crossed bars. The ferrule is shown as (f). With an arm length of $|ac| = |df| = 10mm$, the parallel bars of $|bd| = |ce| = 11mm$ mounted at $|bc| = |de| = 4mm$, the ferrule can extend up to a radius of $27mm$, while the (c) and (d) axis are located only at a radius of $10mm$ when the positioner is folded in. However, the fully extended position is a singularity and the configuration of the robot becomes unstable. The range has to be limited to some degree, to avoid this instability. Considering a pitch of $26mm$, the mechanical envelope of the pivots (c) and (d) could have a diameter of $6mm$. Using smaller pivots, the pitch can be reduced, and the positioner can reach even past the center of its neighbours. In this case a coverage like the tilting spines (figure 4.2 bottom) could be achieved. The actuator could be mounted on the axis of pivot (b) or (c).

This numerical example shows that the cross-arm geometry relaxes the constraint of having small actuators for the beta-axis while giving a much better focal plane coverage than the $\alpha - \beta$ geometry. The drawback of this geometry is an increased mechanical complexity. The positioning accuracy is also harder to achieve as there are more parts and interfaces involved.

4.1.2 Design elements for the $\alpha - \beta$ geometry

Actuators

This subsection discusses the choice of rotatory actuators which are used in the $\alpha - \beta$ geometry and the rotational part of the $R - \Theta$ geometry. Possible technologies for the actuator include stepper, brushless DC and piezo motors. Brushed DC motors are not considered because their performance is affected by wear of the brushes within the required lifetime. Additionally the wear of the brushes generates dust particles which could end up on the telescope mirrors.

- Stepper motor

  Stepper motors have the characteristic of having a passive holding torque. The consequence is that when the power is turned off, they can only stop at a full step. This requires a very high reduction ratio, for example a
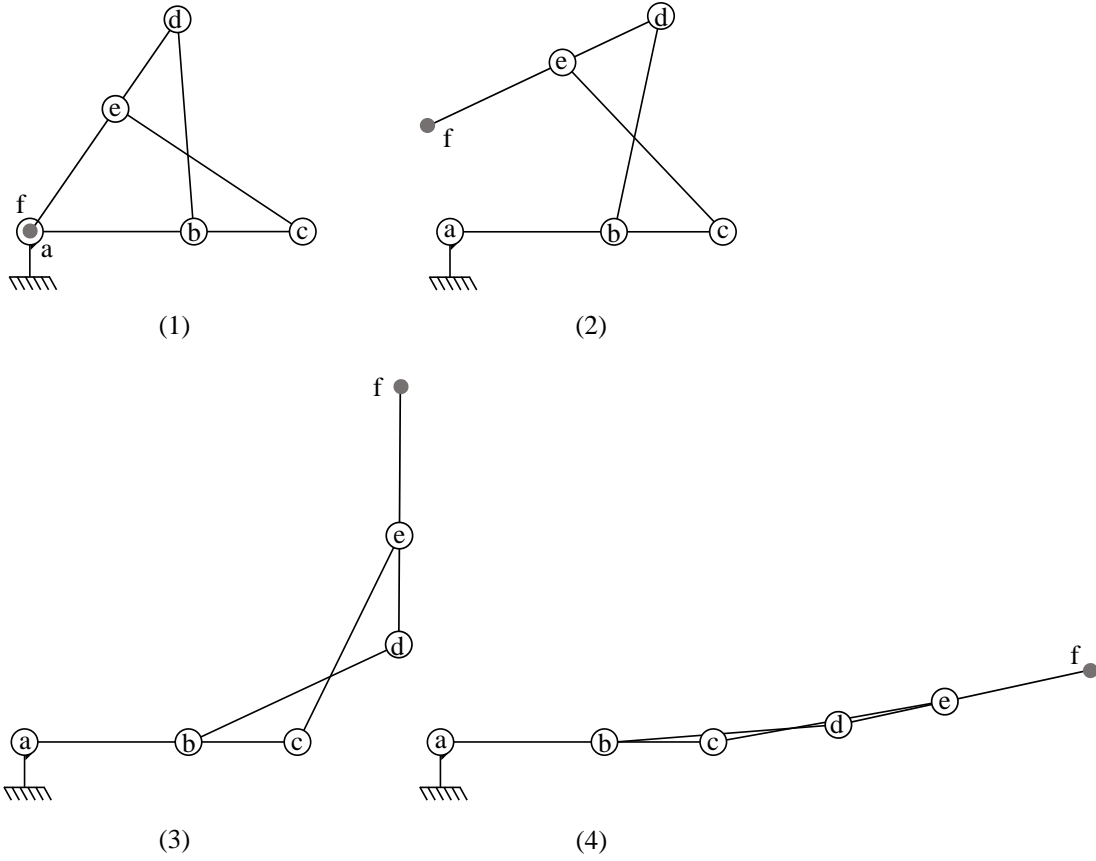
Figure 4.4: Folding-out sequence of the cross-arm geometry. In (1) the positioner is completely folded in and the ferrule (f) is at its center (a). As the positioner folds out through states (2) and (3) to (4), the distance of the ferrule from the center is increasing. The first actuator would be located on the axis (a) and makes the positioner rotate around it's center axis (not shown in this sequence). The second actuator would be located on the axis (b) or (c) and defines the radial position of the ferrule.

ratio of at least 500:1 is needed for a motor with 20 steps per turn. An exception is the variable reluctance type of stepper motor which however is hard to miniaturize and is not available in the small size required for fiber positioners. It is a common misconception that the passive holding torque helps the positioner to keep its position during the exposure of the telescope: The high ratio gearheads are not backdrivable, and provide by themselves the needed passive holding torque.

An advantage of the stepper motor is the higher pole number. Typically a stepper motor has 20 poles whereas a brushless DC motor typically has only 1. This increases inherently the positioning resolution.

Another advantage is the relatively low cost compared to brushless DC motors.

Usually, a stepper motor needs 4 wires to operate: two per phase. In the $\alpha - \beta$ geometry, this can be a disadvantage as the wires of the upper motor have to run through the hollow shaft along with the fiber. One way to eliminate one wire is to connect one end of each phase together to a fixed voltage of $V_{in}/2$. The other two ends can be driven between 0 and V_{in}. In this way the phase voltage range is reduced to $\pm V_{in}/2$ but the stepper motor can be used with 3 wires.
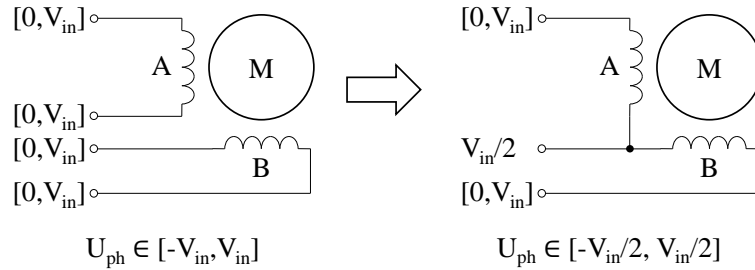
Figure 4.5: Method to reduce the number of wires from 4 to 3 for a stepper motor.

There are standard stepper motors available down to $\varnothing$6mm from Faulhaber.

- Brushless DC motor

    A brushless DC motor has no passive holding torque. Using a vectorial position control can therefore be applied to increase the positioning resolution. However the motor will not keep its position by itself

    The construction of this motor type is well adapted for down-scaling: The smallest standard brushless DC motors are $\varnothing$4mm (ref Faulhaber, Maxon, Namiki) and $\varnothing$2mm prototypes are already available (ref Namiki).

- Piezo motor

  We can identify two types of rotary piezo motors: Ultrasonic and 'Walking' type. In the ultrasonic type, a standing wave is generated in the stator by piezoelectric elements. This generates small incremental movements in the rotor. In the 'walking' type, groups of piezoelectric elements fixed in the stator, 'walk' like legs on the rotor shaft, making it turn.

  Both types have in common that they rely on friction to transmit motion and have therefore a low repeatability. However, they have a very high resolution and they have a passive holding torque, which allows them to drive a positioner in direct drive (without gear transmission).

  The smallest standard 'walking' type motor is ∅17mm from Faulhaber. The smallest ultrasonic type motor is ∅2.4mm, developed by Newscale for the Cobra fiber positioner [16].

Reduction gears

In the case of stepper and brushless DC motors, a reduction gear with a high reduction ratio is generally used. There are two reasons for a high ratio:

- A high ratio increases the positioning resolution. Whether a sensor is used on the motor side or an open loop solution is chosen, the positioning resolution is multiplied by the reduction ratio. (The accuracy however will be limited by backlash and nonlinearities in the gearbox).

- A high gear ratio makes the reduction gears not back drivable and the gearhead will provide the holding torque passively when the power is turned off.

Another important feature is backlash reduction. This can be achieved in serveral ways:

- The gearheads themselves are backlash reduced by preloading two spurgear trains against each other. The preload can be made more precisely, the more stages there are. Therefore, the backlash will be reduced best with a high reduction ratio. Residual hysteresis of $< 0.05°$ are typically achieved.

- The use of a torsion spring at the output of the gearhead which can take out the backlash of the last few stages of the gearhead. Because the gearheads are not backdrivable it is not possible to take out the backlash of the first stages. A residual backlash of $0.1°$ can be achieved.

- A simpler way to deal with the backlash is to use a friction element on the output shaft. This will keep the position passively but the hysteresis of the gearhead still remains. This means that the correction moves (if any) have to go back and forth at least the amount of the hysteresis which is typically around 2°.

Motion control

An open or closed loop control strategy can be used to drive the motors. In both cases a vector control should be used on the stator coils to set the angle of the magnetic field. In the case of an open loop control, the angle of the magnetic field is set to the angle of the trajectory. The current is set to a fixed value. In case of a closed loop control, the magnetic field is set to ±90° with respect to the angle of the rotor to maximize its efficiency. The applied current is proportional to the torque which is the output of a PID position controller. The closed loop control is inherently more energy efficient and can be more reliable, but requires the presence of a position sensor. These considerations are specific to brushless DC motors and stepper motors.

Efforts to achieve sensorless position detection on a brushless DC motor have been made [42], but they rely on the presence of iron in the motor stator. In the case of small size motors, which are iron-less, new efforts are necessary.

Calibration

An important step in achieving high accuracy positioning is the calibration of each positioner. This is especially important if there is no metrology system for closed loop correction moves available. The following lines describe how to calibrate an $\alpha-\beta$ positioner, but similar calibrations are also done for tilting spine and starbugs positioner.

The rigid body model of the positioner is a 2 degree of freedom SCARA kinematics with slightly tilted axes. In addition to the rigid body model it is important to measure the nonlinearity of the actuators. What we mean by this is the difference between a commanded angle and the actual angle on the output of the actuator. These differences have their origin in manufacturing tolerances in the gears of the transmission and geometrical errors in the motor windings and permanent magnets. As the nonlinearity is unique to each actuator, it has to be calibrated for each positioner.

We have shown that the effect of the nonlinearity on the fiber position is larger than the typical precision requirement. However it is repeatable and can therefore be calibrated for. An example of the nonlinearity of one ∅8mm actuator is shown in figure 4.6. Note that the amplitude ($\sim 300\mu$m) is an order of magnitude larger

than the required precision, but the repeatability is 1.5μm. It can be observed that the amplitude of the nonlinearity decreases with frequency. A Fourier transform of the signal, shown if figure 4.7, shows that over 200Hz (meaning 200 periods on one full revolution of the robot arm), the amplitude remains under 1μm. We therefore conclude that the calibration can be done with 200 points per circle.
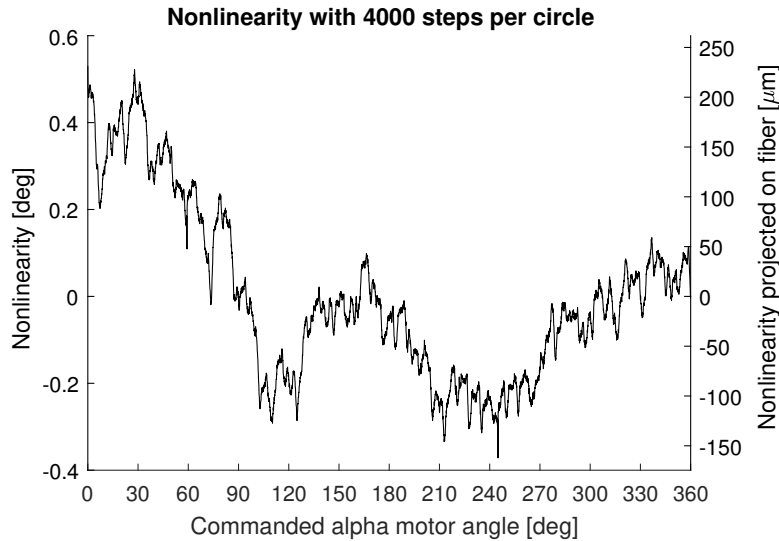
Figure 4.6: Example of nonlinearity of an actuator measuring 4000 steps on one revolution.

Micro switches

Each axis can be equipped with a micro switch which gives it an absolute reference position. With these micro switches, the positioner can recalibrate itself without the need of an external calibration system. Commercially available switches have a diameter of 5mm and an actuation repeatability of 1μm. The rotational movement is converted into a translational movement via an inclined surface and a transfer ball. Figure 4.8 shows the implementation of the switches. Both switches are fixed to the alpha arm (rotate with the alpha axis) and make contact to the base of the positioner and the beta arm.

The motion range of both axes is more than 360° which allows the micro switches to be placed near both ends of the motion range. In this way they can be used as soft stop before the hard stop. This can be useful to prevent hitting the hard stop in case of wrong motor commands. On the other hand it is also useful to place the micro switch in the middle of the motion range. Especially if an absolute recalibration is necessary between each repositioning. In addition, a
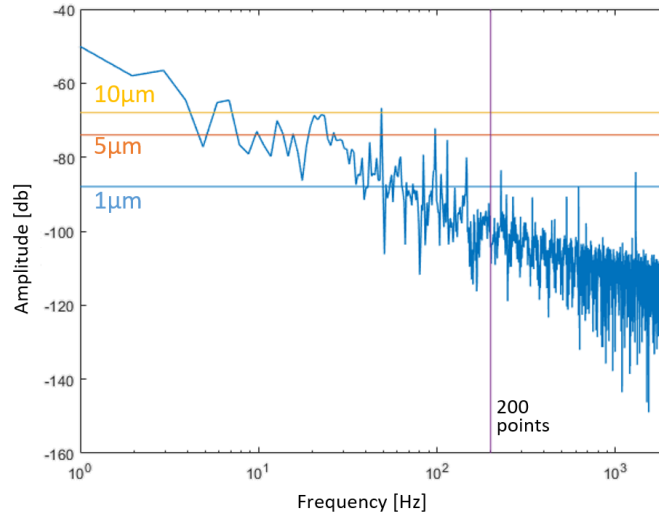
Figure 4.7: FFT of a nonlinearity of an actuator.

calibration position with collision potential is to be avoided in the case of the beta axis.

Alignment of the axes

The alignment of the two rotation axes is the most critical part of the mechanical design. A definition of the axes is given in figure 5.3. As the tilt error of the ferrule will be a sum of manufacturing tolerances on all parts and interface errors between all parts between the focal plate and the ferrule, the number of parts (and therefore interfaces) should kept at a minimum. Additionally, the parts which are critical for the alignment are designed for precise machining: Ideally the interface features are machined as the last operations on the part and on the same machine to minimize machining errors.

Both axes are defined by two widely spaced and preloaded deep groove ball bearings. The axial preload is achieved by compressing an elastic spring washer which is mounted with the bearings and a spacer. A nut secures this assembly. The nut is locked against a hardstop and the compression of the spring washer is defined by the dimensions of the parts for simple assembly. An illustration is given in Figures 4.9 and 4.10.

Flexible coupling

Both rotation axes are well defined by two preloaded bearings. If the actuators were connected directly to the axes, the additional bearing of the gearhead output
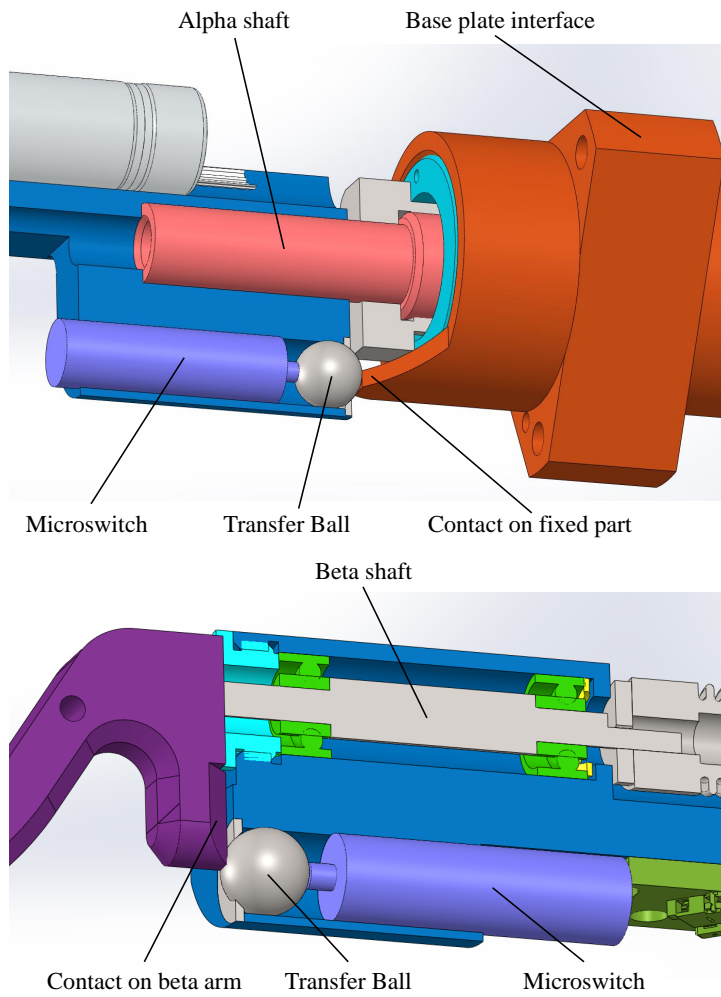
Figure 4.8: Partial cut views of the alpha (top) and beta (bottom) switch implementation.
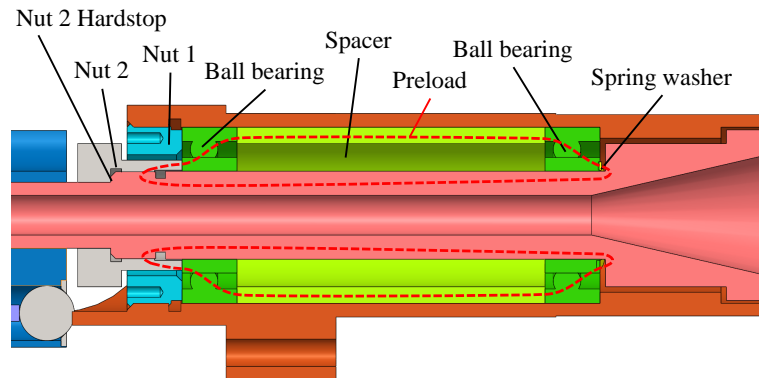
Figure 4.9: Preload of the alpha axis bearings. Nut 1 secures the spacer and the outer rings of the bearings to the chassis. Nut 2 is locked against a hardstop on the hollow shaft and creates the preload via the inner rings of the bearings and the spring washer.
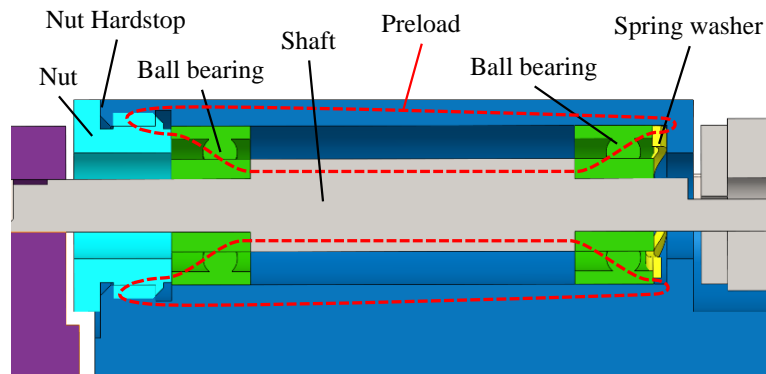
Figure 4.10: Preload of the beta axis bearings. The nut is locked against a hardstop on the housing and creates the preload via the inner rings of the bearings and the spring washer.

would over constrain the axes and the alignment precision would be deteriorated. A solution is to use a flexible coupling which is compliant for tilt, radial and axial misalignments between the gearheads and the axes, but is stiff in torsion and has no backlash. Another solution is to us a long and thin shaft between the actuator and the bearing-guided shaft. This is more cost effective, but has the disadvantage of having a low torsional stiffness.

4.2 Technological limitations

The reason why MOS is used, is that many science cases need a large number of observations of a certain type. In general the more spectra are measured, the more precise the conclusions will be. The goal for any MOS instrument is therefore to measure as many spectra as possible in parallel. This section discusses the limitations to the number of fibers in a fiber positioning system.

4.2.1 Density limit due to telescope

One limit comes from the target density in the field of view of a telescope. A telescope will project only a finite number of targets to the focal plane. This number is limited by the field of view and the light gathering power of the telescope. Obviously it makes no sense to install more fibers than this number. In addition, the targets are rarely distributed uniformly across the field of view. The density of targets has to match the density of fibers also in less dense regions of the field, otherwise the instrument becomes inefficient as fibers in less target-dense regions remain unused for science. If the targets are typically clustered and not distributed uniformly across the field, a lower density, but more flexible solution like the starbugs positioners may be better adapted.

4.2.2 Miniaturization of positioners

From the instrument point of view, the number of fibers is limited by the pitch and the size of the focal plane as seen in section 2.1. The smallest currently existing fiber positioners can accommodate a pitch of around 7mm: The ECHIDNA tilting spine positioners have a pitch of 7,2mm, The $\alpha - \beta$ positioner Cobra has a pitch of 8mm. Concepts like the MOHAWK tilting spine positioner with a pitch of 6.75mm and the $\alpha - \beta$ type positioner presented in section 5.2 with a pitch of 7.375mm exist as prototypes.

Figure 4.11 shows the smallest existing instruments: FMOS with the ECHIDNA positioners, PFS with the Cobra positioner, 4MOST (also ECHIDNA based) and DESI. DESI is currently the instrument with the most fibers. In order to increase

the number to 20'000 we can either increase the focal plane surface or decrease the positioner pitch. We can see that with a circular focal plane with a diameter of 1200mm, the existing ECHIDNA and the 7mm positioner can reach a number exceeding 20'000 fibers. On the other hand, with a hypothetical 5mm pitch, we can reach the same number with a focal plane of ⌀800mm.

The down-scaling from 25mm to 7mm has shown that the loss of angular accuracy due to smaller actuators is compensated by the shorter arm lengths of the smaller geometry. Also the tilt error of the fiber did not increase. What prevented us from making it even smaller was the availability of small and thin ball bearings, and the necessity to assemble the fiber from the back, passing the ferrule through the hollow shaft. If the fiber could be assembled from the front (and then spliced at the back like in DESI [35]), the hole of the hollow shaft could be made smaller. By using custom made, thin bearings on the α axis, a pitch of 5mm should be possible using the 2mm actuators. The bearings would need to have an inner diameter of 1.6mm and an outer diameter of 3.5mm. Further work is necessary to confirm this hypothesis.

The rigidity of the fiber itself does not scale with the positioner. The mechanical effects of the fiber were not negligible already with the 7mm positioner. If we go smaller, these effects will become even bigger.

If a telescope is purposely built for fiber-based spectroscopy, a large focal plane size can be chosen which reduces the need for miniaturization of positioners. Future telescopes concepts with focal plane diameters of up to 1300mm exist already [34].
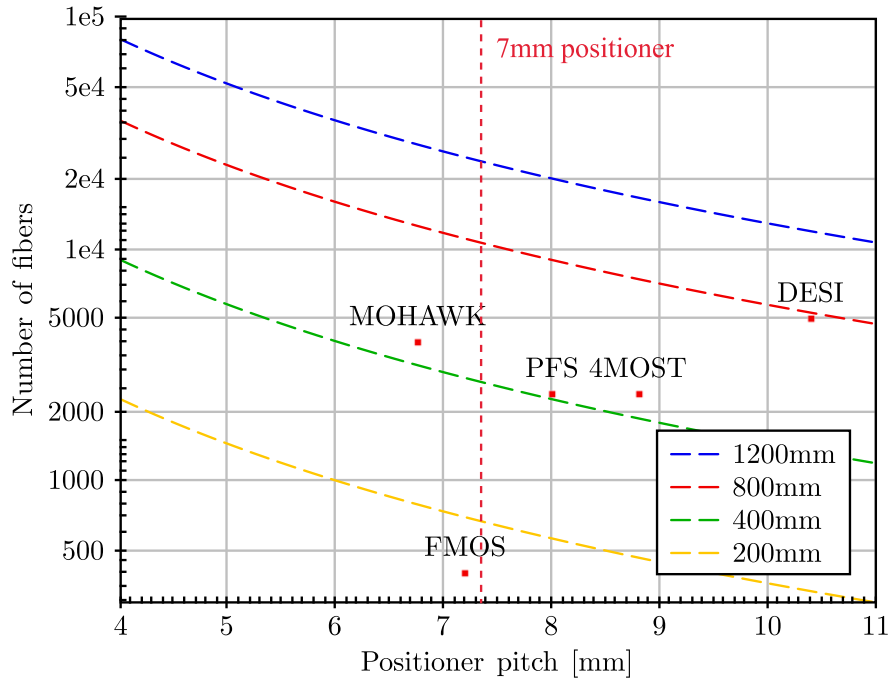
Figure 4.11: Number of fibers in function of positioner pitch for different focal plate sizes. Some existing instruments are shown as examples and the red dashed line is where the 7mm positioner presented in this work would be placed.

Chapter 5

Positioners developments

In this chapter the detailed description of two fiber positioning robots we have developed is given. The first positioner has 25mm diameter and has been developed in the context of the project MOONS. The second positioner has 7mm diameter and it is the smallest developed positioner in its geometry category ($\alpha - \beta$ geometry).

5.1 First positioner: 25mm

Content of this section is based on a work submitted for publication: "High Density Fiber Postitioner System for Massive Spectroscopic Surveys", Authors: Hörler P., Kronig L., Kneib JP., Bouri M., Bleuler H. and von Moos D.

5.1.1 Mechanical design

The kinematics of the positioner is a SCARA-like planar configuration with two rotational degrees of freedom. It allows the movement of the optical fiber in the X and Y directions. An overview of the positioner is shown in figure 5.1. The two axes, α and β, are nearly parallel. α is in the center of the workspace and β is 8mm eccentric as shown in Figure 4.1. The first arm is 8 mm long and the second arm is 17 mm long. The workspace of the positioner has annular shape with an outer diameter of 25 mm and an inner diameter of 9 mm. Both axes have a motion range of more than 360° in order to reach any position in the workspace in left- or right-handed configuration. Mechanical hardstops are implemented to prevent winding up of the fiber. Figure 5.2 shows the hardstop on the alpha axis. The floating green part is necessary to achieve a motion range of more than 360°. The alpha axis has a hollow shaft for the fiber to go through. As opposed to having the fiber outside the positioner, this minimises the bending of the fiber and removes
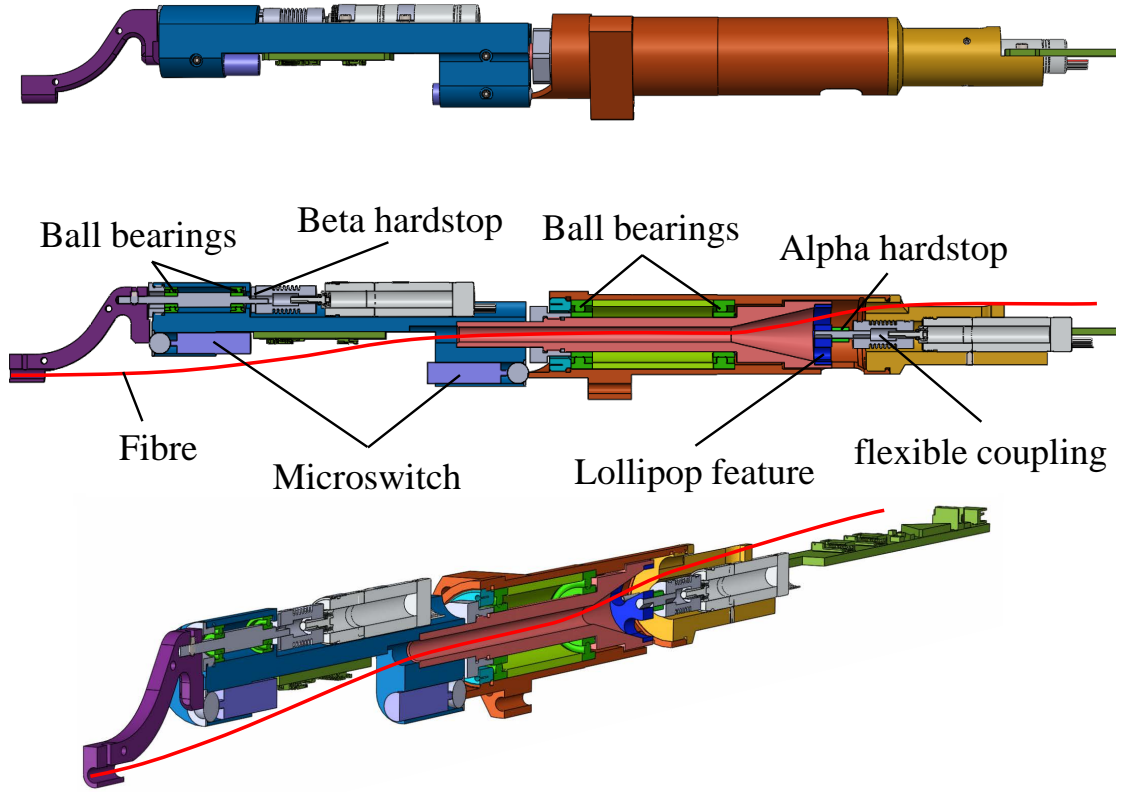
Figure 5.1: Cut View of the positioner. The path of the fiber is shown in red.

any risk of adjacent fibers colliding. Unfortunately, there is no standard hollow shaft motor-gearhead combination available in this size. To overcome this, the lollipop feature is implemented. It transmits the rotation of the actuator to the hollow shaft via just one radial connection. This allows the fiber to pass from the hollow shaft to the side of the actuator.

Actuators

The chosen actuators are identical on the alpha and beta axis. They are ⌀8mm brushless DC motors (type 0824K006B) in combination with 650:1 ratio, backlash reduced planetary gearheads (type 08/3) from the Faulhaber company.

Tilt of the axes

The ferrule has always to be aligned with the chief ray of the light that it captures. The focal surface of this light, defined by the telescope and the corrector optics, can be approximated by a sphere with a radius of $\sim$ 4m. To account for this
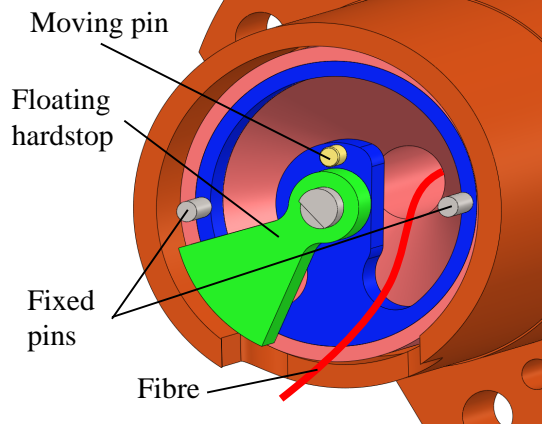
Figure 5.2: Cut View of the positioner revealing the hardstop of the alpha axis and the lollipop feature.

curvature, the physical focal plate is curved and adjacent positioners are tilted by 0.35° to each other. This is more than twice of the tilt error requirement. Therefore, this curvature has to be accounted for even within the workspace of a positioner. While the alpha axis is perpendicular to the focal plate, the beta axis is tilted to the alpha axis by 0.11° and the ferrule is tilted to the beta axis by 0.24°. These angles are illustrated in figure 5.3. By tilting the beta axis and the ferrule, the ferrule will always follow the focal surface and be aligned with the chief ray.
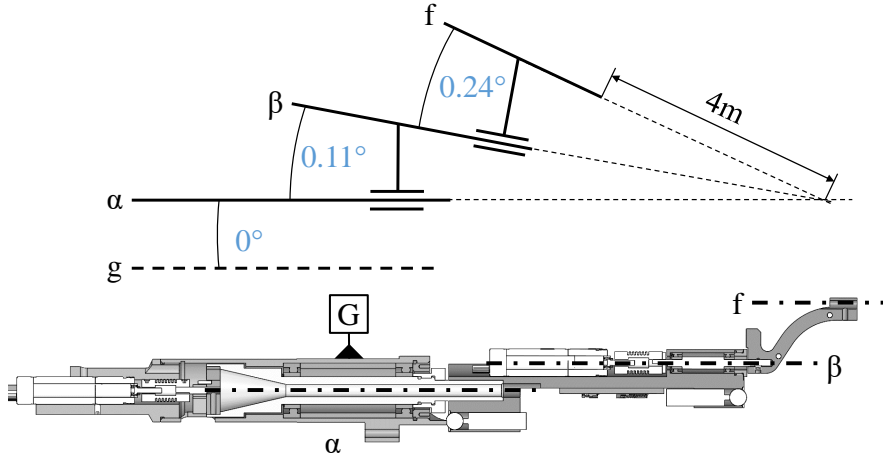
Figure 5.3: Tilt definitions (The angles are exaggerated in this figure).

59

Figure 5.4: Picture of the integrated drive electronic for the 25mm prototype

Fiber/cable path

The fiber and the cables of the beta motor and microswitches are routed through the positioner using a hollow shaft for the alpha axis. As the alpha motor and gearhead do not have a hollow shaft, the fiber and calbes have to be routed out of the rotating hollow shaft using the lollipop feature. As can be seen in figure 5.2, the blue part connects the central shaft of the actuator to the hollow shaft using only one radial connection. In this way, the fiber and cables are pushed a little to the side only at the end of the motion range of the alpha axis.

5.1.2 Drive electronics and software

Each positioner has its own local electronic board. The task of this board is to control both motors, read sensors and communicate with a central unit. The board is attached at the back of the positioner and has to fit into the space envelope of the positioner. As the positioner and electronic board become a single unit, the number of wires connecting each positioner to the central unit is kept to a minimum. The processing unit of the board is a STM32F405 micro controller. It features a CAN interface for the communication, timers for PWM signal generation, GPIO pins and ADCs to read out sensors and enough memory to store trajectories. A picture of the a prototype board is shown in Figure 5.4. The board fulfils the following tasks.

- Position control of both actuators

- Trajectory interpolation

- Communication

- Bootloader

A block diagram of the code in the micro controller is shown in figure 5.5.
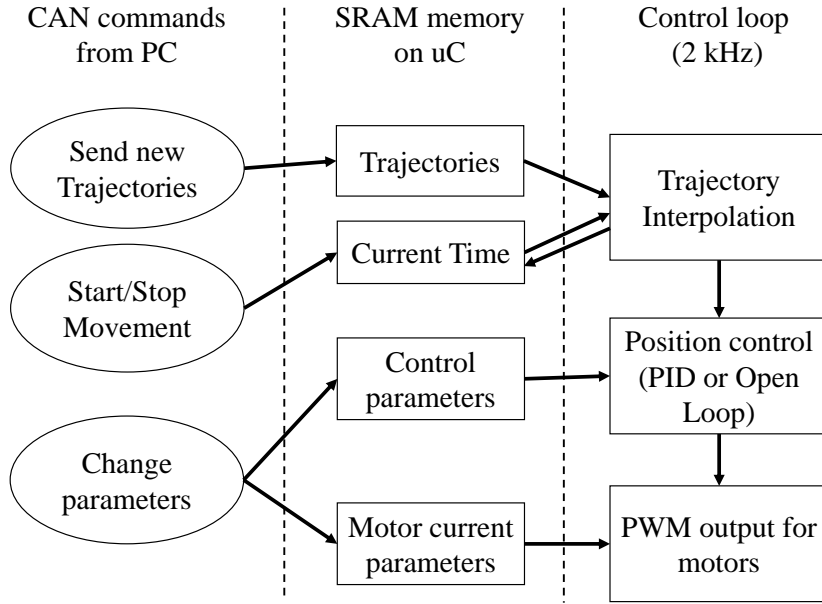
Figure 5.5: Block diagram of the code executed in the micro controller

Communication

The central unit has to send various commands (status requests, motor control parameters, Request to go to datum) and trajectories for both motors. The micro controller has to answer to status requests, notify when movements are completed and send error reports.

The communication with the central unit is realized using a CAN bus. Multiple positioners share a common bus and the central unit can send individually addressed messages or broadcast messages to all positioners on the bus. A CAN bus for the 10 prototype positioners has been realized and tested. For the case of 1000 or more positioners, multiple CAN busses have to be implemented because the CAN bus is physically limited to $\sim$ 150 devices. A solution using 4 embedded PCs as intermediate layer is proposed in figure 5.6. Each embedded PC communicates with the central unit via Ethernet and manages 5 CAN busses with 50 positioners on each CAN bus. The number of Embedded PCs in the intermediate layer and the number of CAN busses per Embedded PC can easily be increased for a larger number of positioners.
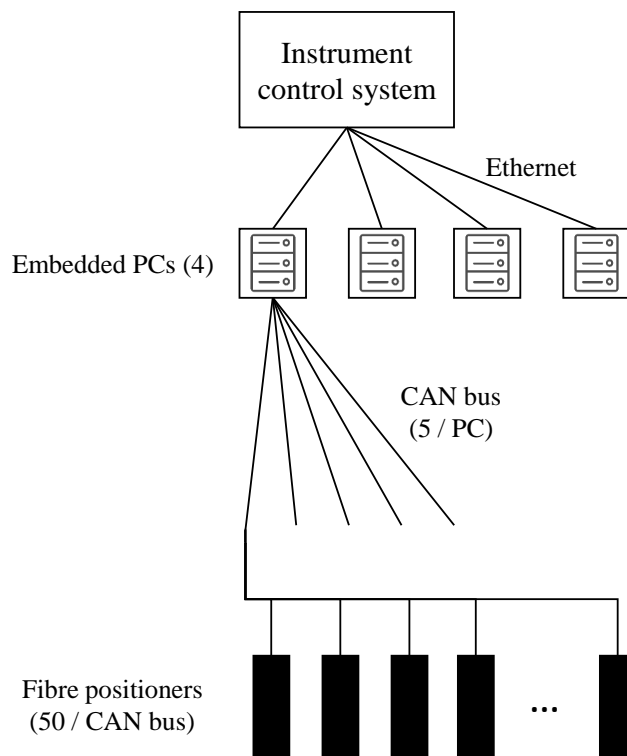
Figure 5.6: Proposed architecture for the communication with 1000 positioners

Trajectory interpolation

The two trajectories (one for each motor) sent to the positioner consist of a set of points $p_i = (t_i, \theta_i)$ where t_i are the time coordinates and θ_i the angle coordinates. The micro controller interpolates linearly between those points to create a trajectory with constant velocity segments. The simplest trajectory, a constant velocity until the target, consists of only one final point; only two 32bit numbers. If there is a need to ramp-up to higher velocities and/or maneuvers for collision avoidance, the trajectory can be made of any number of points (the RAM memory of the micro controller can store several thousand points). However, keeping the number of points low reduces the required time to send the trajectories to the positioners.

Observation sequence

A typical observation block consists of a 10 min to 1 hour exposure in a certain area of the sky. During the exposure, the position of the fibers has to be kept and the power of the positioners is shut down. Each observation block is prepared in advance by selecting the targets, assigning them to positioners and generating

the trajectories using the collision avoidance algorithm. Due to changing weather conditions, observation blocks have to be interchangeable. Therefore each block starts and ends with the positioners in the home position. Figure 5.7 shows the typical operation sequence between two operation blocks on the instrument control system and the positioner electronic board.
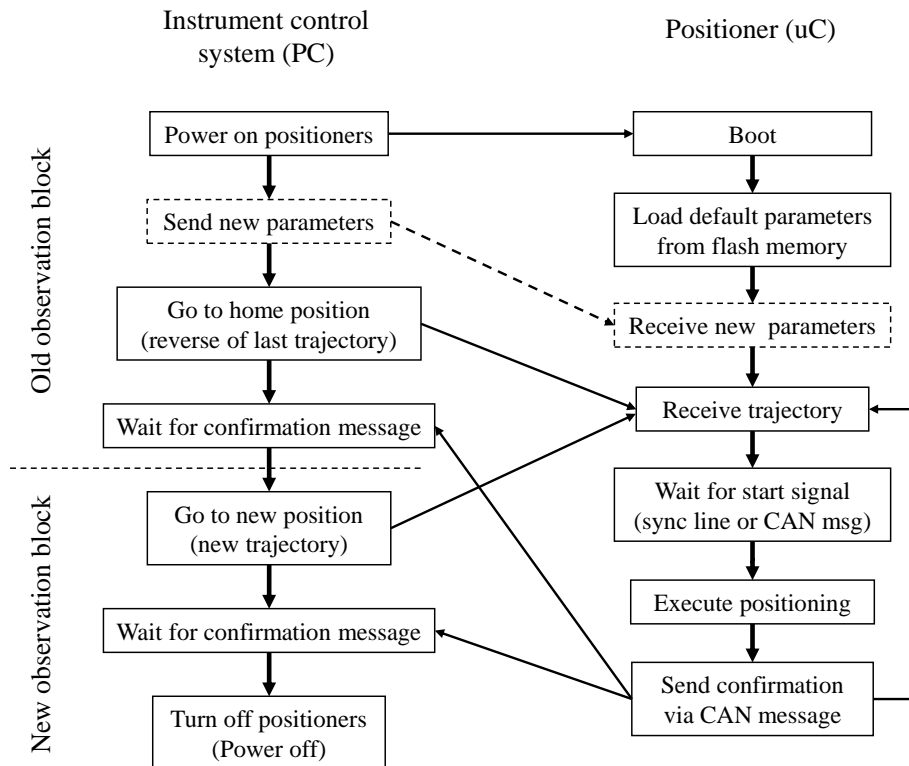
Figure 5.7: Typical operation sequence between two observation blocks

Bootloader

Flashing a firmware to the micro controller requires a jTag or a serial connection from a PC and cannot be done via CAN bus directly. If for some reason the firmware has to be updated when the instrument is already assembled, the positioners have to be removed from the focal plate in order to access the electronics board. This is a complex operation requiring several weeks of downtime. Therefore, a bootloader allowing to reprogram the micro controller via the CAN bus has been implemented. In this way, a firmware update can be deployed within hours without disassembling the instrument.

During assembly, only the bootloader will be flashed to the micro controller from a PC via jTag. The bootloader is a standard program which boots on the micro controller and initializes the CAN communication to a central unit. The central unit can send a new firmware which the bootloader will write to the flash memory of the micro controller. The bootloader then starts the main program. This allows reprogramming of all positioners without physical intervention. A simplified block diagram of a firmware update via CAN bus using the bootloader is shown in figure 5.8. In this example, the sync line (an additional wire) is used to tell the positioners during boot if a firmware update is necessary.

This bootloader has been successfully implemented and is currently being used on the positioners of the DESI instrument [43].

5.2 Second positioner: 7mm

This section describes the development of a positioner with 7.25 mm outer diameter. It is an attempt to create the smallest $\alpha - \beta$ type positioner by miniaturizing the design of the 25 mm positioner using 2 mm brushless gearmotors as actuators. It keeps all the main features, excluding the micro switches.

5.2.1 Mechanical design

The kinematics of the positioner is a SCARA-like planar configuration with two rotational degrees of freedom. It allows the movement of the optical fiber in the X and Y directions. An overview of the positioner is shown in figure 5.9. The two axes, α and β, are parallel. α is in the center of the workspace and β is 2.375 mm eccentric. Therefore the alpha arm is 2.375 mm long and the beta arm is 5 mm long. The workspace of the positioner has annular shape with an outer diameter of 14.75 mm and an inner diameter of 5.25 mm. The α axis has a motion range of more than 360°, while the β axis has a motion rage of 300°. This allows the positioner to reach any position in the workspace, but only in a right-handed configuration. Mechanical hardstops are implemented to prevent winding up of the fiber as shown in figures 5.10 and 5.11. The alpha axis has a hollow shaft for the fiber to go through as opposed to having the fiber outside the positioner. This minimises the bending of the fiber and removes any risk of adjacent fibers colliding. Unfortunately, there is no standard hollow shaft motor-gearhead combination available in this size. To overcome this, the lollipop feature is implemented. It transmits the rotation of the actuator to the hollow shaft via just one radial connection. This allows the fiber to pass from the stationary lower part to the rotating hollow shaft.

Micro Controller

Power on

Bootload? (Sync line high) — No → Set the execution pointer to the main application

Yes

Send ready message

Remove write protection for flash pages 62 - 255, Receive code size and number of parts

Erase Flash pages 62 - 255 (Main application), Part counter = 0

Send "ready for part n" message. Receive part and write to Flash

Read flash and send back to PC

Verification Ok? — Not Ok

Ok

All parts written? — No → Increment Part counter

Yes

Set write protection for flash pages 62 -255

Send confirmation to PC

PC

Set Sync line high

Power on positioners

Wait for ready message

Send code size and number of parts

Part counter = 0

Receive "ready for part n" message. Send part of code

Receive verification and send result back — Not Ok

Ok

All parts written? — No → Increment Part counter

Yes

Wait for confirmation of positioner

Turn power off

CAN communications

65

Figure 5.8: Simplified block diagram of a firmware update via CAN bus using a bootloader.
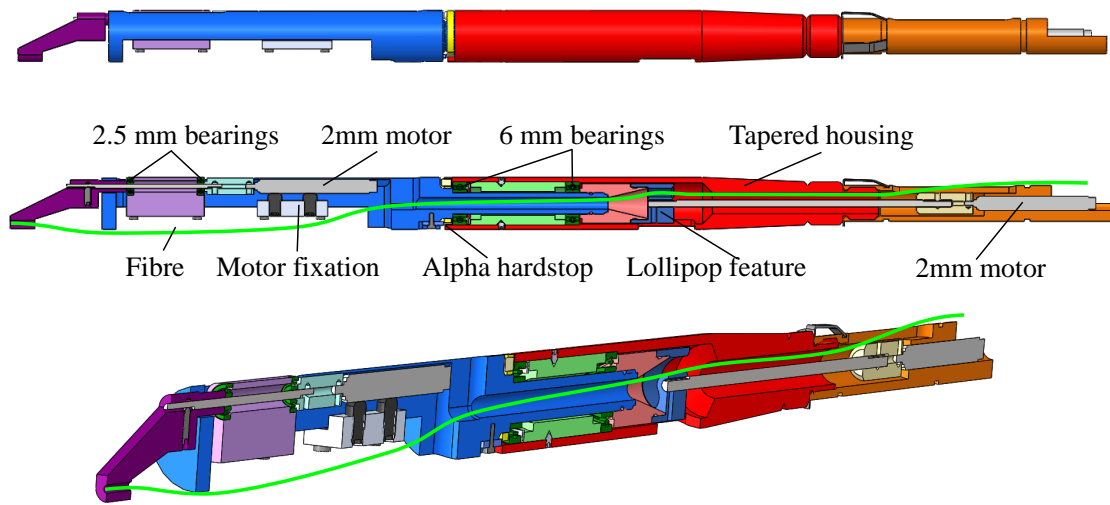
Figure 5.9: Overview of the 7mm positioner
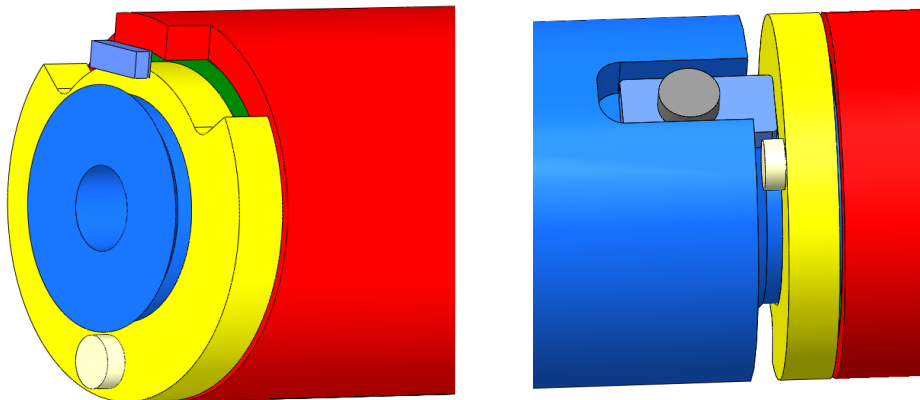
Figure 5.10: Cutview and detail of the alpha hardstop. The red part is the stationary lower housing. The yellow ring, including the light yellow pin, can rotate freely for about 40° around the blue hollow shaft. The rotation of the upper housing is limited by the light yellow pin.
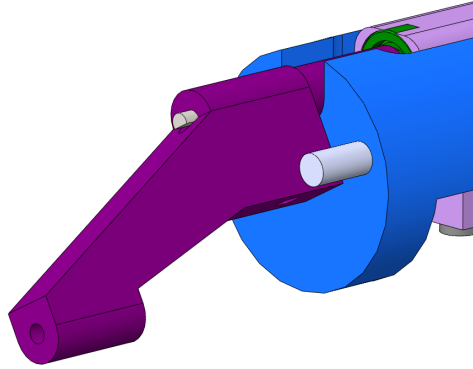
Figure 5.11: Detail of the beta hardstop. The rotation range of the beta arm is limited by the light gray dowel pin.

Tilt of the axes

For this positioner, the axes are kept parallel. As the tilt correction of the axes is proportional to the arm lengths (small angles approximation), it can be neglected for these short arm lengths. For a telescope focal length of 4m, the corrections would only be 0.034° and 0.072°.

Alignment of the axes

As for the 25mm positioner, the axes are guided using 2 axially preloaded deep groove ball bearings. Moreover, the number of parts between the support plate and the fiber is kept to a minimum and the mechanical design of the parts is such that the important interfaces can be manufactured with the highest precision.

The bearings for the beta axis have an outer diameter of 2.25 mm and are bigger than the actuator. In an attempt to maximise the alpha arm length - and thus minimise the arm ratio - the bearings are mounted against a V-groove in the upper housing. This solution has been proven to be insufficient for the alignment of the axis because the upper housing is not stiff enough. An alternate solution houses the bearings in the mounting block as shown in figure 5.12.

The coupling between the axes and the actuators is a rigid coupling. The compliance of the thin (and long in the case of the alpha axis) shafts is large enough to allow for misalignments of the gearhead output shaft.

Actuator choice

The actuators of this prototype are brushless DC motors with 1:1024 planetary gearheads of an outer diameter of 2 mm and provided by Namiki. The gearheads
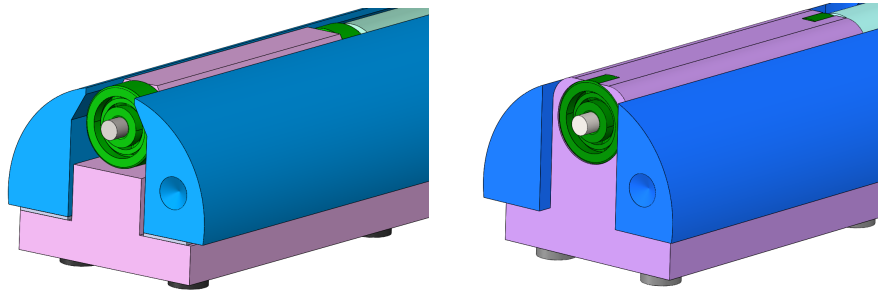
Figure 5.12: Mounting of the bearings for the beta axis. The blue part is the upper housing, the pink part is the mounting block and the green parts are the ball bearings. *Left:* Initial mounting of the bearings for the beta axis against a V-groove in the upper housing. *Right:* Improved mounting of the bearings for the beta axis using a mounting block.

have no backlash reduction and present a $\sim 2°$ backlash. Most of this backlash is however taken out by friction in the bearings as long as the targets are always approached from the same side.

Fiber/cable path

As in the 25-mm positioner, the fiber is routed through the positioner using a hollow shaft for the alpha axis. This requires the use of the lollipop feature.

Chapter 6

Positioners performance

In this chapter our test setups and calibration protocols are presented. The performance results of the two positioners are discussed.

6.1 Test methods

Two test setups have been used for the evaluation of performance: A position bench and a tilt bench. They are briefly presented here and are described in more details in [28].

Position bench

The first setup measures the XY position of the fiber using a backlit multimode fiber and a camera in front of the positioner (figure 6.1 middle). The absolute X/Y accuracy of this setup is of 1μm.

Tilt bench

The second setup is an optical bench which allows simultaneous measurement of the position of the fiber and its tilt anywhere in the workspace. A backlit single mode fiber emits a cone of light through a lens on a screen located at the focal length of the lens. In this way, the position of the light on the screen gives the tilt of the fiber independently of the position of the fiber as shown in figure 6.1 (top). The tilt θ of the fiber is given by

$$\theta = arctan\left(\frac{\Delta x}{f}\right) \tag{6.1}$$

where Δx is the displacement on the screen (in 2 dimensions) and f the focal length of the lens. A second camera measures the position by seeing the fiber
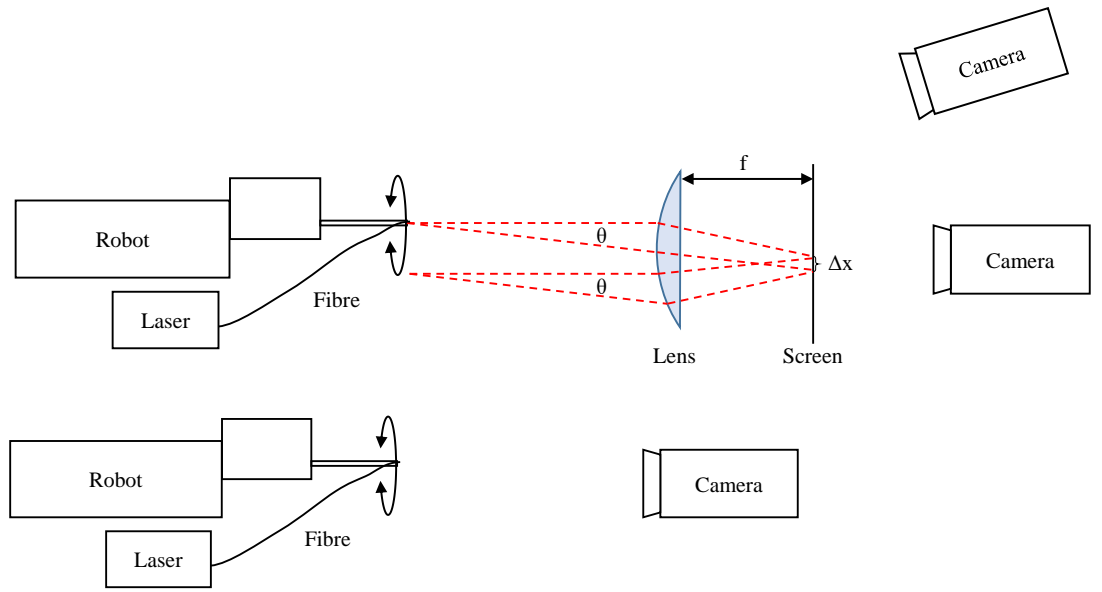
Figure 6.1: Principle of the tilt bench (top), principle of the XY bench (middle) and a top view of the tilt bench (bottom).

directly without using the screen. The XY position precision is of 10μm and the tilt precision is of $0.01°$.

Calibration

The position and tilt measurements are used to calibrate the prototypes. The rigid body model of the positioner is a 2 dof SCARA kinematics including the tilt of the axes. In addition, the nonlinearity of the actuators is measured as well. The calibrated parameters are:

- Location of alpha axis (center of positioner)
- Alpha and beta arm length
- Angular position of alpha and beta micro switch

- Tilt of the alpha axis with respect to the base plate

- Tilt of the beta axis with respect to the alpha axis

- Tilt of the ferrule with respect to the beta axis

- Nonlinearity of the gearmotors

The protocol for the calibration is as follows: the alpha and beta actuators are driven to certain angles and the resulting XY position and tilt of the fiber is measured. The calibration points are chosen to cover the whole workspace evenly. Each actuator is doing full revolutions, while the other actuator is fixed in different positions. A certain number of points are measured on these revolutions. This allows us to estimate the nonlinearity of each actuator.

After all points are measured, the rigid body model is fitted onto all points using a nonlinear least squares optimization.

For the nonlinearity, the error with respect to a perfectly linear actuator is stored for each measured calibration point. For the angles between the calibration points, the correction is approximated using a linear interpolation between two adjacent points.

We cannot fit a model of the nonlineartiy of the actuators, because it is a random signal. The origin of the nonlinearity lies in geometrical imprecisions in the reduction gears and motor windings. The theoretical model would be a combination of periodic signals where the frequency depends on which reduction stage they are created. Because we use high ratio reduction gears, this results in too many parameters and even the shape of the periodic signals is unknown.

The error between the measured points and the calibrated model, gives an indication of how well the positioner will perform in the XY positioning test.

By repeating the measurements at the same points, we can measure the repeatability in position and tilt. And by approaching each point from both directions, we can measure the hysteresis in the actuators.

XY positioning Test

The calibrated model is used to generate motor commands for a grid of test targets as illustrated in figure 6.2. The positioner is then driven to those targets and the position of the fiber is measured. Any residual hysteresis is avoided by approaching the target always from the same side. It has to be noted that the resulting XY positioning accuracy is achieved in open loop, without the use of a metrology system for correction moves.
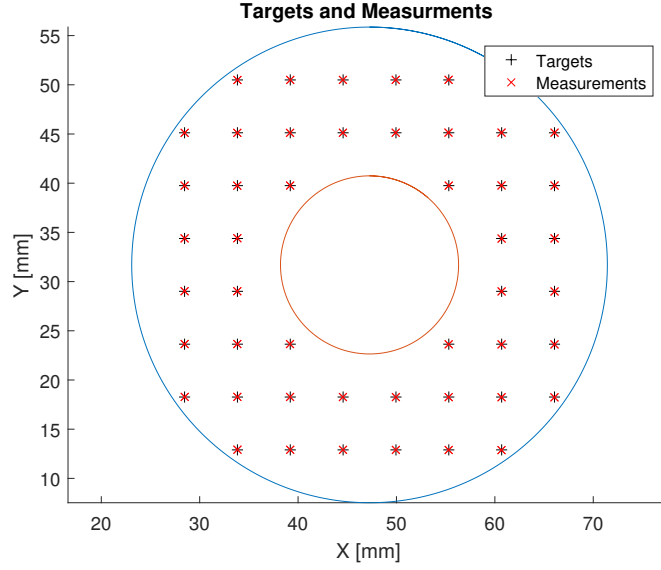
Figure 6.2: Grid of test targets and corresponding measurements. The limits of the workspace are indicated by the 2 circles.

6.2 Prototype performance: 25mm prototypes

In order to evaluate the performance of the positioner design, 10 prototypes have been built according to the mechanical design presented in section 5.1.1 and using the drive electronics presented in section 5.1.2. The actuators used are 8mm brushless motors with backlash free reduction gears (preloaded double spur gear train) with a ratio of 650:1.

6.2.1 Positioning performance

Accuracy

For each of the 10 prototypes, the RMS of the absolute error is shown in figure 6.3 (top). Prototypes 6 and 9 are missing because their reduction gears were damaged and the preload for the backlash reduction is missing. The average Error is 20μm with a standard deviation of 3.9μm. 5 of the remaining 8 would fulfil the XY accuracy requirement of the MOONS project. This result is obtained without feedback of a metrology system.
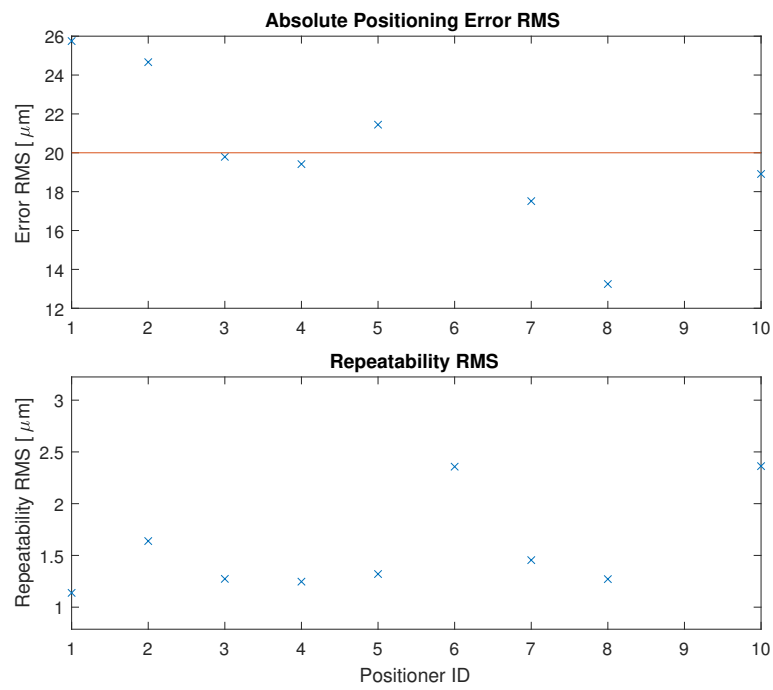
Figure 6.3: Absolute accuracy of positioning and repeatability for the 10 proto-types

Repeatability

Each target of the XY positioning test is visited multiple times and therefore the repeatability in positioning can be measured on each of these points. Figure 6.3 (bottom) shows the RMS of the repeatability for the 10 prototypes. Note that most positioners are repeatable to the precision of the test bench which is around $1 \mu m$

Hysteresis

The hysteresis of each axis is measured by approaching all points of the calibration procedure from either side. The difference in position of the measurements is then converted into an angle on the actuator axis. Similar to the nonlinearity, each transmission has a different hysteresis curve within the revolution. The average of all motors is $0.039°$ with a standard deviation of $0.035°$.

It can be observed that with an arm length of 25mm, a hysteresis of $0.039°$ translates to an error of 17 μm, however the maximum values are around 60 μm. This is 3 times the required accuracy. Therefore, even with the backlash reduced gearheads, it is still necessary to approach the targets always from the same side. Thanks to the still relatively low hysteresis, this can be done by an additional back and forth movement at the end of the generated trajectory, without the need of running the collision avoidance algorithm again.

Datum switch repeatability

The Datum switches are an absolute reference for the positioner. By running against the switches it is able to recalibrate its position in case some steps were lost during observation or after a power failure. The precision of subsequent positioning depends (among other factors) on the precision of this switch. The precision of the alpha switch has been measured by repeatedly running the positioner against the switch and recording its position each time. The histogram of the deviation from the mean position is shown in figure 6.4. The RMS value is 0.7 μm which lies within the measurement precision of the XY test bench.

6.2.2 Tilt performance

The tilt of the fiber relative to the reference, in this case the baseplate, can be measured directly at different positions in the workspace. The tilt of both axes and fiber relative to each other have to be estimated using a rigid body model of the positioner as mentioned in section 6.1. Table 6.1 shows an example of results for one of the 10 prototypes. The fit of the model to the measured points has an
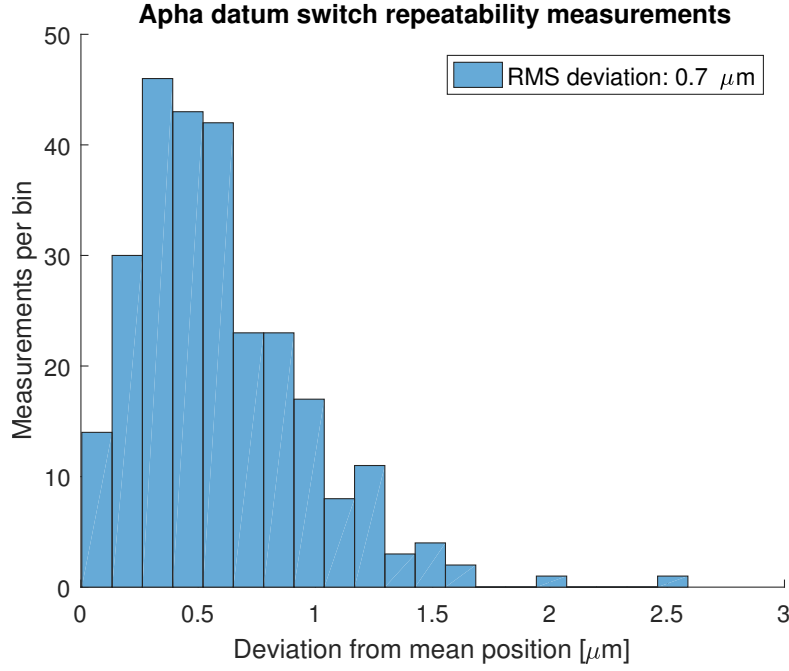
Figure 6.4: Datum switch repeatability

rms error of 0.016° which is just slightly larger than the precision of the tilt bench. This means that the rigid body model represents well the real positioner.

Using the identified model of the positioner (including the relative tilts between the axes), it is possible to predict the total tilt error of the fiber in all possible configuration of the positioner. Figure 6.5 shows all possible errors of the two axes and the ferrule for this positioner. The alpha axis has always the same tilt error as it does not move. The beta axis however is rotating around the alpha axis and its tilt error describes a circle around the tilt error of the alpha axis. The ferrule in turn rotates around the beta axis and its tilt error can be anywhere in the green surface. This example shows that the maximum tilt error is around 0.14°. This is the worst case configuration of the positioner where all the tilt errors add up. In the best case configuration, the 3 tilt errors cancel out and the tilt error of the fiber is 0°.

The alpha - beta and beta - ferrule tilt errors are shown for all 10 prototypes in figure 6.6. The ground - alpha tilt error is not reported because the fixation of the positioners on the test bench was not repeatable enough and therefore this measurement was not consistent. The average alpha - beta tilt error is 0.04° with a standard deviation of 0.02°. The average beta - ferrule tilt error is 0.14° with a standard deviation of 0.14°.

It has to be kept in mind that the tilt error requirement of 0.15° concerns the

Angles [deg]	Target	Measured	Difference
g to α (Orientation)		350.2	
g to α	0	0.033	0.033
α to β (Orientation)	180	203.2	23.2
α to β	0.11	0.046	0.064
β to f (Orientation)	180	167.7	12.3
β to f	0.24	0.208	0.032

Table 6.1: Example of a tilt measurement

sum of these 3 errors. The alpha - beta tilt error of most positioners is of less than a third of the requirement. The beta - ferrule tilt error however lies over the overall tilt requirement for half of the positioners. This poor performance can be attributed to the ferrules themselves which show a misalignment of the fiber with respect to the outside diameter of up to several tenths of degrees. It is also possible that the two interfaces of the beta arm (to the beta axis shaft and ferrule) do not guarantee a good alignment in which case the interfaces have to be improved by making them longer or using a V-groove. It can be expected that the ground - alpha tilt error has a similar magnitude than the alpha - beta tilt error, because there is only one part involved (the base of the positioner) which has relatively large interface surfaces. The alignment of the alpha axis on one positioner was measured to be 0.03° using a Coordinate-measuring machine during assembly.

These hypotheses have to be confirmed by additional tests using an improved interface on the test bench and measuring the tilt errors of the ferrules themselves.

6.2.3 FRD due to fiber stress

The throughput loss due to focal ratio degradation within the fiber has been measured on one prototype. The throughput is compared between the fiber alone, the fiber in the positioner at minimal bending (beta arm folded in) and the fiber in the positioner at maximal bending (beta arm stretched out). The difference between the 3 cases is less than 1% which is the accuracy of the measuring device. Further testing has to be done to confirm the requirement of 0.5%.

6.2.4 Collision avoidance

The collision avoidance algorithm has been validated on a sample of 10 positioners. The 10 prototypes are mounted on a test plate with 37 holes, arranged in a 25 mm pitched hexagonal pattern. The trajectories generated by the collision avoidance algorithm are sent to the positioners via the CAN bus described in section 5.1.2.
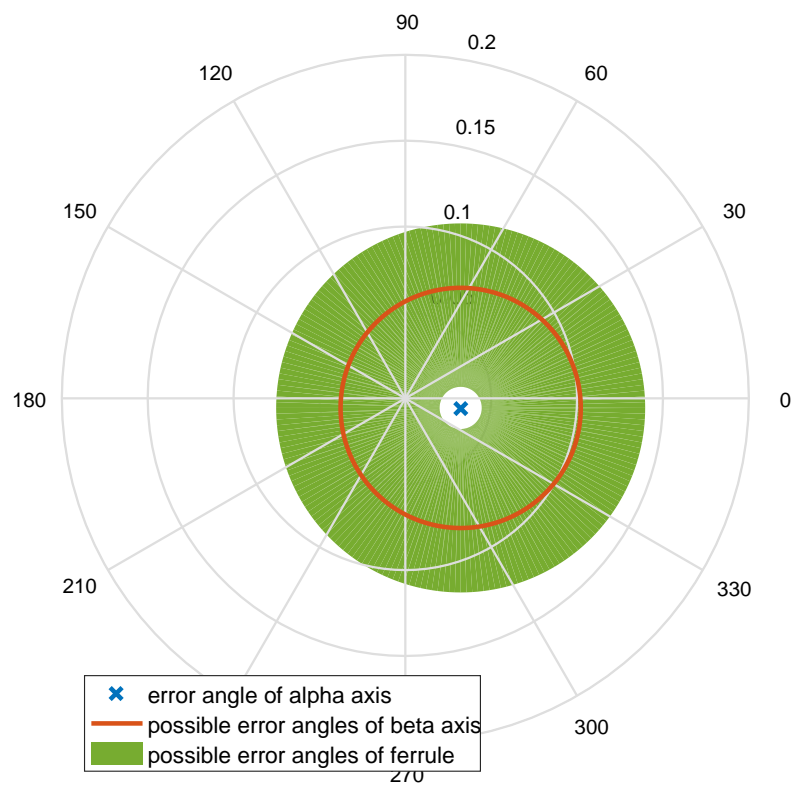
Figure 6.5: Example of tilt errors in all possible configurations
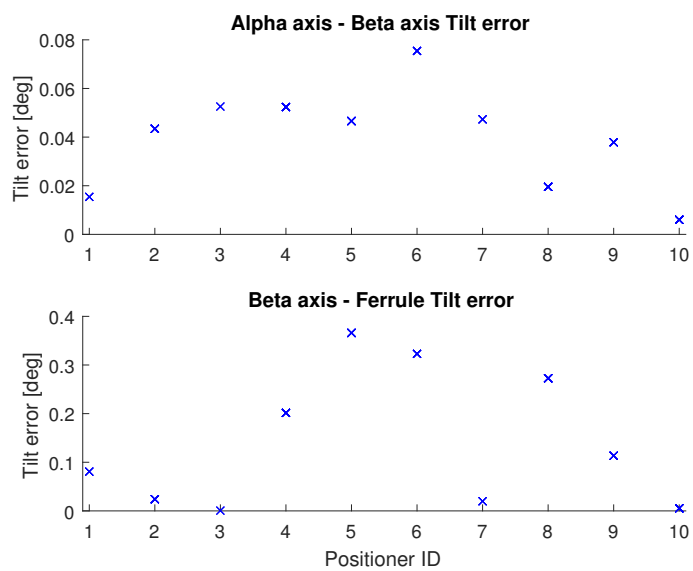
Figure 6.6: Tilt errors alpha - beta and beta - ferrule for the 10 prototypes
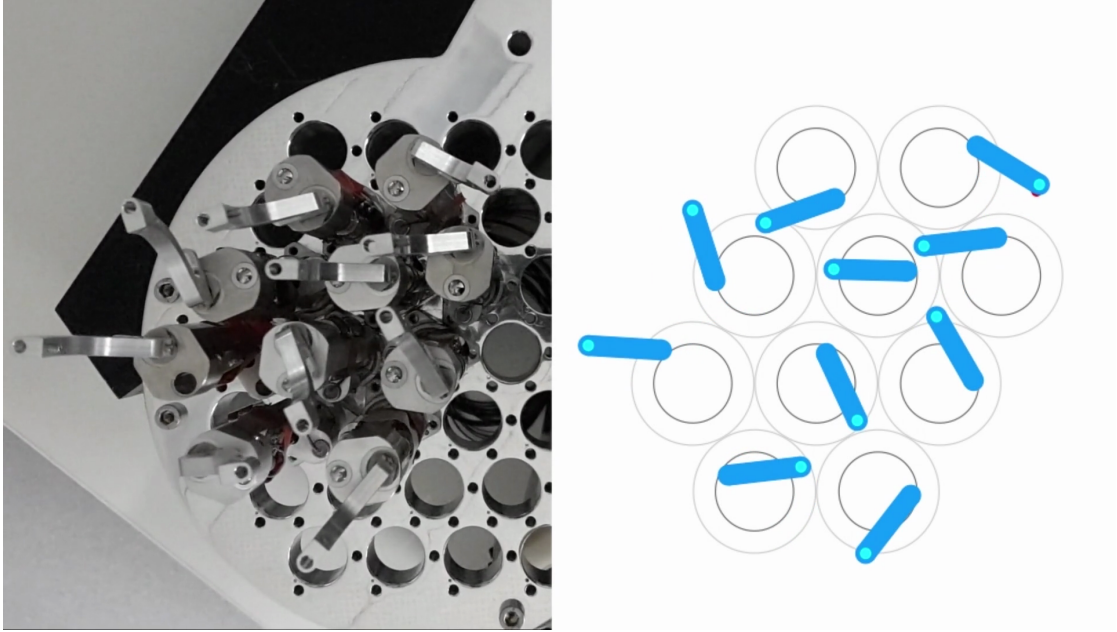
Figure 6.7: Snapshot of a collision avoidance test run. Right side: Simulation of trajectories at target positions. Left side: Execution of these trajectories with 10 prototypes. The full video can be seen at: https://youtu.be/Hc_Pr_hhaNA

A broadcast CAN message then starts the movements on all positioners at the same time.

All the tested trajectories were successfully executed without collisions and the communication worked as expected. Figure 6.7 shows the 10 prototypes at their assigned target locations.

6.2.5 Summary

Table 6.2 compares the obtained results with the requirements of the MOONS project. The mass of the positioner has been measured to be 164.5g including motors, electronics and wiring. The operational temperature and humidity, max Z error and lifetime have not yet been tested.

6.3 Prototype performance: 7mm prototype

In order to evaluate the performance of the positioner design, 1 prototype has been built according to the mechanical design presented in section 5.2.1 and using the same drive electronics as the 25mm prototype presented in section 5.1.2. The

Requirement	Value	Achieved performance
Focal plane coverage	Each position reachable by at least 2 positioners	Verified by design
Minimal fiber distance	4mm	Verified by design
Pitch	25mm	Verified by design
Size of the pupil	610μm	Verified by design
Lifetime	10^6 Movements / 10 years	
Reconfiguration time	< 30 sec	25 sec
RMS XY Error	$< 20\mu$m	20μm
Z max defocus error	$< 50\mu$m	
Max tilt error	$\pm 0.15°$	cf. section 6.2.2
FRD due to fiber stress	$< 0.5\%$ throughput loss	cf. section 6.2.3
Difference in focal ratio between fiber input and output	$< 1\%$	Verified by design
Operational temperature	$-10°$C to $+30°$C	
Operational humidity	5% to 20%	
Power while active	< 2W	1.5W
Power while inactive	0W	0W
Mass of the positioner	< 200g	164.5g

Table 6.2: Fiber positioning requirements and achieved performance
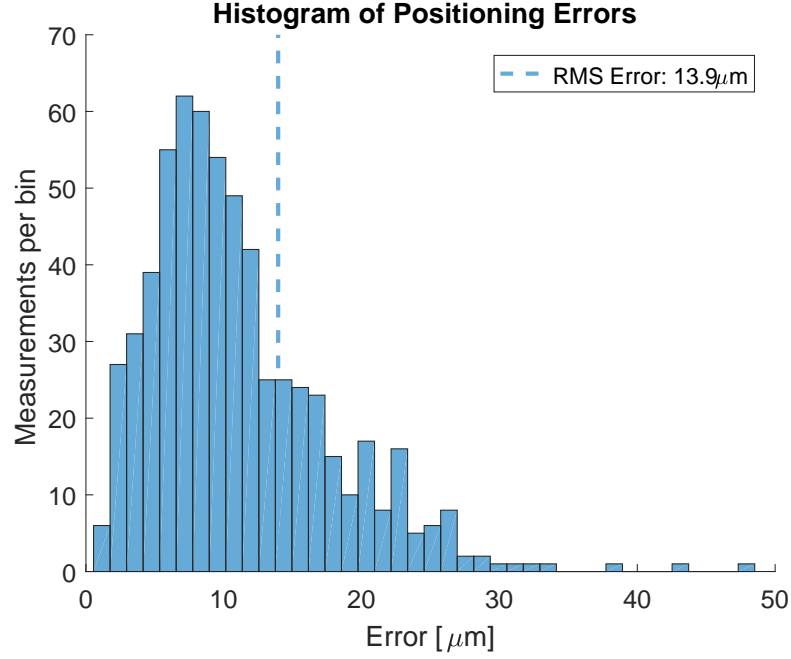
Figure 6.8: Histogram of the absolute errors in the XY positioning test of the 7mm positioner.

actuators used are 2mm brushless motors with 5 stage planetary gearheads with a ratio of 1024:1. The gearheads are not backlash-reduced.

6.3.1 Positioning performance

Accuracy

The histogram of the absolute errors in the XY positioning test is shown in figure 6.8. The RMS Error is 13.9μm with a standard deviation of 8.2μm. This result is obtained without feedback of a metrology system. The XY positioning of the 7mm design is therefore more accurate than the one of the 25mm design. This is mostly due to the shorter arm lengths. The angular accuracy of the actuators is less good as manufacturing tolerances in the motor and gearheads do not scale with size and become larger relative to the size of the actuator.

Repeatability

Each target of the XY positioning test is visited multiple times and therefore the repeatability in positioning can be measured on each of these points. The RMS of the repeatability at all targets is 6.5μm. The 7mm design is therefore less precise
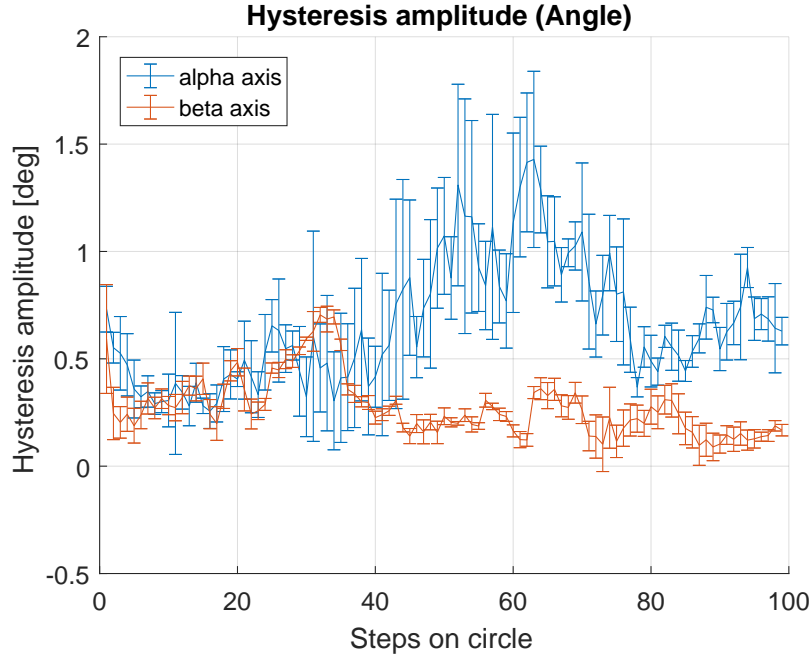
Figure 6.9: Hysteresis of both axes over one revolution. The error bars correspond to the standard deviation across different measurements.

than the 25mm design. This can be explained with the fact that non-repeatable friction in the gearhead and the external bearings have a bigger effect at smaller scale.

Hysteresis

The hysteresis of the two actuators is shown in figure 6.9. As expected, the absence of a backlash reduction in the gearheads leads to a hysteresis of up to 1.5° on the alpha axis. With a radius of 7.375mm (at the outer edge of the workspace), this corresponds to 193μm at the fiber. This means that for correction moves of a few μm at the targets, the fiber has to go back and forth 200μm. Also, during the trajectory, the collision avoidance algorithm has to respect a large margin around each beta arm. Alternatively, an external backlash reduction mechanism using a torsion spring could be implemented.

6.3.2 Tilt performance

The tilt of the fiber relative to the reference, in this case the baseplate, can be measured directly at different positions in the workspace. The tilt of both axes and fiber relative to each other have to be estimated using a rigid body model

81

Angles [deg]	Measured Amplitude	Orientation
g to α	0.070	91.7
α to β	0.116	312.3
β to f	0.081	0

Table 6.3: Tilt measurements of the 7mm prototype. The target tilt is 0° (parallel axes).

of the positioner as mentioned in section 6.1. Table 6.3 shows the measured tilt angles. The fit of the model to the measured points has an rms error of 0.047° which is just slightly larger than the precision of the tilt bench. This means that the rigid body model represents well the real positioner.

Using the identified model of the positioner (including the relative tilts between the axes), it is possible to predict the total tilt error of the fiber in all possible configuration of the positioner. Figure 6.10 shows all possible errors of the two axes and the ferrule for this positioner. The alpha axis has always the same tilt error as it doesn't move. The beta axis however is rotating around the alpha axis and its tilt error describes a circle around the tilt error of the alpha axis. The ferrule in turn rotates around the beta axis and its tilt error can be anywhere in the green surface. This example shows that the maximum tilt error is around 0.27°. This is the worst case configuration of the positioner where all the tilt errors add up. In the best case configuration, the 3 tilt errors cancel out and the tilt error of the fiber is 0°.

This result shows that the alignment of the axes in the 7mm design is not very good, but sufficient for some applications. Potential to improve lies is the mounting of the beta axis bearings and the ferrules themselves as stated in section 5.2.1.

6.3.3 Summary

Table 6.4 compares the obtained results with the requirements of the MOONS project. The mass of the positioner has been measured to be 11.1g including motors and wiring, excluding the electronics. The operational temperature and humidity, max Z error and lifetime have not yet been tested.
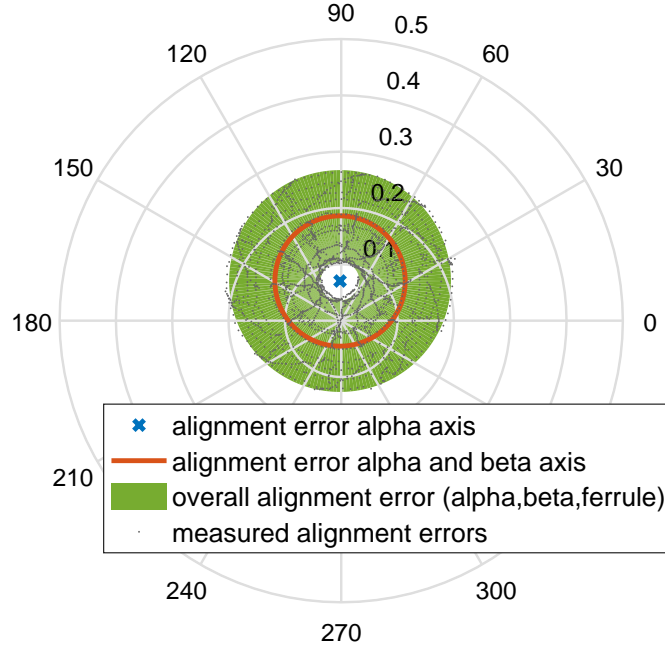
Figure 6.10: Tilt errors in all possible configurations

Requirement	Value	Achieved performance
Focal plane coverage	Each position reachable by at least 2 positioners	Verified by design
Minimal fiber distance	2mm	Verified by design
Pitch	7.375mm	Verified by design
Lifetime	10^6 Movements / 10 years	
Reconfiguration time	< 30 sec	20 sec
RMS XY Error	$< 20\mu$m	13.9μm
Z max defocus error	$< 50\mu$m	
Max tilt error	$\pm 0.15°$	0.27°
FRD due to fiber stress	$< 0.5\%$ throughput loss	
Operational temperature	$-10°$C to $+30°$C	
Operational humidity	5% to 20%	
Power while active	< 2W	2.5W
Power while inactive	0W	0W
Mass of the positioner	< 200g	11.1g

Table 6.4: Fiber positioning requirements and achieved performance

Chapter 7

Conclusions and future work

The coming years will see significant progress in optical and IR astronomical instrumentation. One of the new technologies are massively parallel fiber positioners in the focal plane of large telescopes. Several international consortia are working on such projects. We at EPFL are concentrating on the fiber positioners themselves and their collision avoidance algorithms, other groups are concerned with integration, fiber systems, spectrographs etc. At EPFL, three PhD theses are being carried out; collision avoidance (Makarem [30]) optical test benches and motor control (Kronig) and this work focussing on the design of the two-degree-of-freedom positioners themselves. The challenge is to design high-accuracy positioners with very tight size restrictions in view of massively parallel operation and associated assembly questions, all this at a reasonable cost.

The innovative solutions proposed here are mainly in the mechanical design domain, but also in the electronics and control implementations. The thesis aims at providing a comprehensive mechanical analysis on fiber positioners. The theoretical framework derives the mechanical constraints that a fiber positioner has to fulfil from the astrophysical needs. This theoretical framework can be used as a "check list" for future work. Starting from these mechanical constraints and based on our experience in the development of two fiber positioning robots, the corresponding mechanical solutions are described in detail in the chapter of the design guidelines.

We have developed two robots: the ⌀25mm and the ⌀7mm. The development of these two robots is described in detail, accompanied by the results of the performance tests we have conducted. They represent an advancement in particular in terms of accuracy and short reconfiguration time. Moreover, the 7mm represents the current frontier in the development of the smallest fiber positioners within its geometry category. The 7mm maintains high accuracy and short reconfiguration time despite its small size. However, it is more expensive than the 25mm mainly because of the cost of its actuators.

The success of the 7mm robot suggests that the diameter size may be further reduced. Future work may succeed in reducing the size if the shaft can be maintained without losing stiffness. Because MOS surveys need more and more fibers to be positioned very densely, another challenge for future work is to assure industrial production of a large number of very small fiber positioners, considering that the costs entailed are high.

As future surveys may have their telescopes built on purpose for fiber-based spectroscopy, future studies may evaluate the best performing and most cost-effective way to increase the number of fibers, which can go in two directions that are not in alternative: reducing positioner size and increasing focal plane size. To the first extent, this thesis provides an advancement in the current state of the art.

Bibliography

[1] Masayuki Akiyama, Scott Smedley, Peter Gillingham, Jurek Brzeski, Tony Farrell, Masahiko Kimura, Rolf Muller, Naoyuki Tamura, and Naruhisa Takato. Performance of Echidna fiber positioner for FMOS on Subaru. pages 70182V–70182V–12, July 2008.

[2] Lauren Anderson, Eric Aubourg, Stephen Bailey, Florian Beutler, Vaishali Bhardwaj, Michael Blanton, Adam S. Bolton, J. Brinkmann, Joel R. Brownstein, Angela Burden, Chia-Hsun Chuang, Antonio J. Cuesta, Kyle S. Dawson, Daniel J. Eisenstein, Stephanie Escoffier, James E. Gunn, Hong Guo, Shirley Ho, Klaus Honscheid, Cullan Howlett, David Kirkby, Robert H. Lupton, Marc Manera, Claudia Maraston, Cameron K. McBride, Olga Mena, Francesco Montesano, Robert C. Nichol, Sebastian E. Nuza, Matthew D. Olmstead, Nikhil Padmanabhan, Nathalie Palanque-Delabrouille, John Parejko, Will J. Percival, Patrick Petitjean, Francisco Prada, Adrian M. Price-Whelan, Beth Reid, Natalie A. Roe, Ashley J. Ross, Nicholas P. Ross, Cristiano G. Sabiu, Shun Saito, Lado Samushia, Ariel G. Sanchez, David J. Schlegel, Donald P. Schneider, Claudia G. Scoccola, Hee-Jong Seo, Ramin A. Skibba, Michael A. Strauss, Molly E. C. Swanson, Daniel Thomas, Jeremy L. Tinker, Rita Tojeiro, Mariana Vargas Magana, Licia Verde, David A. Wake, Benjamin A. Weaver, David H. Weinberg, Martin White, Xiaoying Xu, Christophe Yeche, Idit Zehavi, and Gong-Bo Zhao. The clustering of galaxies in the SDSS-III Baryon Oscillation Spectroscopic Survey: Baryon Acoustic Oscillations in the Data Release 10 and 11 galaxy samples. *Monthly Notices of the Royal Astronomical Society*, 441(1):24–62, April 2014. arXiv: 1312.4877.

[3] Lauren Anderson, Eric Aubourg, Stephen Bailey, Dmitry Bizyaev, Michael Blanton, Adam S. Bolton, J. Brinkmann, Joel R. Brownstein, Angela Burden, Antonio J. Cuesta, Da Costa, Luiz A. N, Kyle S. Dawson, Roland de Putter, Daniel J. Eisenstein, James E. Gunn, Hong Guo, Jean-Christophe Hamilton, Paul Harding, Shirley Ho, Klaus Honscheid, Eyal Kazin, David Kirkby, Jean-Paul Kneib, Antoine Labatie, Craig Loomis, Robert H. Lupton, Elena Malanushenko, Viktor Malanushenko, Rachel Mandelbaum, Marc

Manera, Claudia Maraston, Cameron K. McBride, Kushal T. Mehta, Olga Mena, Francesco Montesano, Demetri Muna, Robert C. Nichol, Sebastián E. Nuza, Matthew D. Olmstead, Daniel Oravetz, Nikhil Padmanabhan, Nathalie Palanque-Delabrouille, Kaike Pan, John Parejko, Isabelle Pâris, Will J. Percival, Patrick Petitjean, Francisco Prada, Beth Reid, Natalie A. Roe, Ashley J. Ross, Nicholas P. Ross, Lado Samushia, Ariel G. Sánchez, David J. Schlegel, Donald P. Schneider, Claudia G. Scóccola, Hee-Jong Seo, Erin S. Sheldon, Audrey Simmons, Ramin A. Skibba, Michael A. Strauss, Molly E. C. Swanson, Daniel Thomas, Jeremy L. Tinker, Rita Tojeiro, Mariana Vargas Magaña, Licia Verde, Christian Wagner, David A. Wake, Benjamin A. Weaver, David H. Weinberg, Martin White, Xiaoying Xu, Christophe Yèche, Idit Zehavi, and Gong-Bo Zhao. The clustering of galaxies in the SDSS-III Baryon Oscillation Spectroscopic Survey: baryon acoustic oscillations in the Data Release 9 spectroscopic galaxy sample. *Monthly Notices of the Royal Astronomical Society*, 427(4):3435–3467, December 2012.

[4] Samuel C. Barden and Taft Armandroff. Performance of the WIYN fiber-fed MOS system: Hydra. volume 2476, pages 56–67, 1995.

[5] Samuel C. Barden, Taft Armandroff, Gary P. Muller, Andy C. Rudeen, Jeff L. Lewis, and Lee Groves. Modifying Hydra for the WIYN telescope: an optimum telescope, fiber MOS combination. volume 2198, pages 87–97, 1994.

[6] M. Cirasuolo, J. Afonso, M. Carollo, H. Flores, R. Maiolino, E. Oliva, S. Paltani, Leonardo Vanzi, Christopher Evans, M. Abreu, David Atkinson, C. Babusiaux, Steven Beard, F. Bauer, M. Bellazzini, Ralf Bender, P. Best, N. Bezawada, P. Bonifacio, A. Bragaglia, I. Bryson, D. Busher, A. Cabral, K. Caputi, M. Centrone, F. Chemla, A. Cimatti, M-R. Cioni, G. Clementini, J. Coelho, D. Crnojevic, E. Daddi, J. Dunlop, S. Eales, S. Feltzing, A. Ferguson, M. Fisher, A. Fontana, J. Fynbo, B. Garilli, G. Gilmore, A. Glauser, I. Guinouard, F. Hammer, P. Hastings, A. Hess, R. Ivison, P. Jagourel, M. Jarvis, L. Kaper, G. Kauffman, A. T. Kitching, A. Lawrence, D. Lee, B. Lemasle, G. Licausi, S. Lilly, D. Lorenzetti, D. Lunney, R. Maiolino, F. Mannucci, R. McLure, D. Minniti, D. Montgomery, B. Muschielok, K. Nandra, R. Navarro, P. Norberg, S. Oliver, L. Origlia, N. Padilla, J. Peacock, F. Pedichini, J. Peng, L. Pentericci, J. Pragt, M. Puech, S. Randich, P. Rees, A. Renzini, N. Ryde, M. Rodrigues, I. Roseboom, F. Royer, R. Saglia, A. Sanchez, R. Schiavon, H. Schnetler, D. Sobral, R. Speziali, D. Sun, R. Stuik, A. Taylor, W. Taylor, S. Todd, E. Tolstoy, M. Torres, M. Tosi, E. Vanzella, L. Venema, F. Vitali, M. Wegner, M. Wells, V. Wild, G. Wright, G. Zamorani, and M. Zoccali. MOONS: the Multi-Object Optical and Near-

infrared Spectrograph for the VLT. volume 9147, pages 91470N–91470N–13, 2014.

[7] Kyle S. Dawson, David J. Schlegel, Christopher P. Ahn, Scott F. Anderson, Éric Aubourg, Stephen Bailey, Robert H. Barkhouser, Julian E. Bautista, Alessandra Beifiori, Andreas A. Berlind, Vaishali Bhardwaj, Dmitry Bizyaev, Cullen H. Blake, Michael R. Blanton, Michael Blomqvist, Adam S. Bolton, Arnaud Borde, Jo Bovy, W. N. Brandt, Howard Brewington, Jon Brinkmann, Peter J. Brown, Joel R. Brownstein, Kevin Bundy, N. G. Busca, William Carithers, Aurelio R. Carnero, Michael A. Carr, Yanmei Chen, Johan Comparat, Natalia Connolly, Frances Cope, Rupert A. C. Croft, Antonio J. Cuesta, Luiz N. da Costa, James R. A. Davenport, Timothée Delubac, Roland de Putter, Saurav Dhital, Anne Ealet, Garrett L. Ebelke, Daniel J. Eisenstein, S. Escoffier, Xiaohui Fan, N. Filiz Ak, Hayley Finley, Andreu Font-Ribera, R. Génova-Santos, James E. Gunn, Hong Guo, Daryl Haggard, Patrick B. Hall, Jean-Christophe Hamilton, Ben Harris, David W. Harris, Shirley Ho, David W. Hogg, Diana Holder, Klaus Honscheid, Joe Huehnerhoff, Beatrice Jordan, Wendell P. Jordan, Guinevere Kauffmann, Eyal A. Kazin, David Kirkby, Mark A. Klaene, Jean-Paul Kneib, Jean-Marc Le Goff, Khee-Gan Lee, Daniel C. Long, Craig P. Loomis, Britt Lundgren, Robert H. Lupton, Marcio A. G. Maia, Martin Makler, Elena Malanushenko, Viktor Malanushenko, Rachel Mandelbaum, Marc Manera, Claudia Maraston, Daniel Margala, Karen L. Masters, Cameron K. McBride, Patrick McDonald, Ian D. McGreer, Richard McMahon, Olga Mena, Jordi Miralda-Escudé, Antonio D. Montero-Dorta, Francesco Montesano, Demitri Muna, Adam D. Myers, Tracy Naugle, Robert C. Nichol, Pasquier Noterdaeme, Sebastián E. Nuza, Matthew D. Olmstead, Audrey Oravetz, Daniel J. Oravetz, Russell Owen, Nikhil Padmanabhan, Nathalie Palanque-Delabrouille, Kaike Pan, John K. Parejko, Isabelle Pâris, Will J. Percival, Ismael Pérez-Fournon, Ignasi Pérez-Ràfols, Patrick Petitjean, Robert Pfaffenberger, Janine Pforr, Matthew M. Pieri, Francisco Prada, Adrian M. Price-Whelan, M. Jordan Raddick, Rafael Rebolo, James Rich, Gordon T. Richards, Constance M. Rockosi, Natalie A. Roe, Ashley J. Ross, Nicholas P. Ross, Graziano Rossi, J. A. Rubiño-Martin, Lado Samushia, Ariel G. Sánchez, Conor Sayres, Sarah J. Schmidt, Donald P. Schneider, C. G. Scóccola, Hee-Jong Seo, Alaina Shelden, Erin Sheldon, Yue Shen, Yiping Shu, Anže Slosar, Stephen A. Smee, Stephanie A. Snedden, Fritz Stauffer, Oliver Steele, Michael A. Strauss, Alina Streblyanska, Nao Suzuki, Molly E. C. Swanson, Tomer Tal, Masayuki Tanaka, Daniel Thomas, Jeremy L. Tinker, Rita Tojeiro, Christy A. Tremonti, M. Vargas Magana, Licia Verde, Matteo Viel, David A. Wake, Mike Watson, Benjamin A. Weaver, David H. Weinberg, Benjamin J. Weiner, Andrew A. West, Martin

White, W. M. Wood-Vasey, Christophe Yeche, Idit Zehavi, Gong-Bo Zhao, and Zheng Zheng. The Baryon Oscillation Spectroscopic Survey of SDSS-III. *The Astronomical Journal*, 145(1):10, January 2013. arXiv: 1208.0022.

[8] Roelof S. de Jong, Sam Barden, Olga Bellido-Tirado, Joar Brynnel, Cristina Chiappini, Éric Depagne, Roger Haynes, Diana Johl, Daniel P. Phillips, Olivier Schnurr, Axel D. Schwope, Jakob Walcher, Svend M. Bauer, Gabriele Cescutti, Maria-Rosa L. Cioni, Frank Dionies, Harry Enke, Dionne M. Haynes, Andreas Kelz, Francisco S. Kitaura, Georg Lamer, Ivan Minchev, Volker Müller, Sebastián E. Nuza, Jean-Christophe Olaya, Tilmann Piffl, Emil Popow, Allar Saviauk, Matthias Steinmetz, Uğur Ural, Monica Valentini, Roland Winkler, Lutz Wisotzki, Wolfgang R. Ansorge, Manda Banerji, Eduardo Gonzalez Solares, Mike Irwin, Robert C. Kennicutt, David M. P. King, Richard McMahon, Sergey Koposov, Ian R. Parry, Xiaowei Sun, Nicholas A. Walton, Gert Finger, Olaf Iwert, Mirko Krumpe, Jean-Louis Lizon, Vincenzo Mainieri, Jean-Philippe Amans, Piercarlo Bonifacio, Matthieu Cohen, Patrick François, Pascal Jagourel, Shan B. Mignot, Frédéric Royer, Paola Sartoretti, Ralf Bender, Hans-Joachim Hess, Florian Lang-Bardl, Bernard Muschielok, Jörg Schlichter, Hans Böhringer, Thomas Boller, Angela Bongiorno, Marcella Brusa, Tom Dwelly, Andrea Merloni, Kirpal Nandra, Mara Salvato, Johannes H. Pragt, Ramón Navarro, Gerrit Gerlofsma, Ronald Roelfsema, Gavin B. Dalton, Kevin F. Middleton, Ian A. Tosh, Corrado Boeche, Elisabetta Caffau, Norbert Christlieb, Eva K. Grebel, Camilla J. Hansen, Andreas Koch, Hans-G. Ludwig, Holger Mandel, Andreas Quirrenbach, Luca Sbordone, Walter Seifert, Guido Thimm, Amina Helmi, Scott C. trager, Thomas Bensby, Sofia Feltzing, Gregory Ruchti, Bengt Edvardsson, Andreas Korn, Karin Lind, Wilfried Boland, Matthew Colless, Gabriella Frost, James Gilbert, Peter Gillingham, Jon Lawrence, Neville Legg, Will Saunders, Andrew Sheinis, Simon Driver, Aaron Robotham, Roland Bacon, Patrick Caillier, Johan Kosmalski, Florence Laurent, and Johan Richard. 4most: 4-metre Multi-Object Spectroscopic Telescope. volume 9147, pages 91470M–91470M–14, 2014.

[9] Timothée Delubac, Julian E. Bautista, Nicolás G. Busca, James Rich, David Kirkby, Stephen Bailey, Andreu Font-Ribera, Anže Slosar, Khee-Gan Lee, Matthew M. Pieri, Jean-Christophe Hamilton, Éric Aubourg, Michael Blomqvist, Jo Bovy, J. Brinkmann, William Carithers, Kyle S. Dawson, Daniel J. Eisenstein, Satya Gontcho A. Gontcho, Jean-Paul Kneib, J.-M. Le Goff, Daniel Margala, Jordi Miralda-Escudé, Adam D. Myers, Robert C. Nichol, Pasquier Noterdaeme, Ross O'Connell, Matthew D. Olmstead, Nathalie Palanque-Delabrouille, Isabelle Pâris, Patrick Petitjean,

Nicholas P. Ross, Graziano Rossi, David J. Schlegel, Donald P. Schneider, David H. Weinberg, Christophe Yèche, and Donald G. York. Baryon Acoustic Oscillations in the Ly-alpha forest of BOSS DR11 quasars. *Astronomy & Astrophysics*, 574:A59, February 2015. arXiv: 1404.1801.

[10] Scott Dodelson, Katrin Heitmann, Chris Hirata, Klaus Honscheid, Aaron Roodman, Uroš Seljak, Anže Slosar, and Mark Trodden. Cosmic Visions Dark Energy: Technology. *arXiv:1604.07821 [astro-ph]*, April 2016. arXiv: 1604.07821.

[11] Alan Dressler, Tyson Hare, Bruce C. Bigelow, and David J. Osip. IMACS: the wide-field imaging spectrograph on Magellan-Baade. In *Ground-based and Airborne Instrumentation for Astronomy*, volume 6269, page 62690F. International Society for Optics and Photonics, June 2006.

[12] D. J. Eisenstein, I. Zehavi, D. W. Hogg, R. Scoccimarro, M. R. Blanton, R. C. Nichol, R. Scranton, H. Seo, M. Tegmark, Z. Zheng, S. Anderson, J. Annis, N. Bahcall, J. Brinkmann, S. Burles, F. J. Castander, A. Connolly, I. Csabai, M. Doi, M. Fukugita, J. A. Frieman, K. Glazebrook, J. E. Gunn, J. S. Hendry, G. Hennessy, Z. Ivezic, S. Kent, G. R. Knapp, H. Lin, Y. Loh, R. H. Lupton, B. Margon, T. McKay, A. Meiksin, J. A. Munn, A. Pope, M. Richmond, D. Schlegel, D. Schneider, K. Shimasaku, C. Stoughton, M. Strauss, M. SubbaRao, A. S. Szalay, I. Szapudi, D. Tucker, B. Yanny, and D. York. Detection of the Baryon Acoustic Peak in the Large-Scale Correlation Function of SDSS Luminous Red Galaxies. *The Astrophysical Journal*, 633(2):560–574, November 2005. arXiv: astro-ph/0501171.

[13] Daniel J. Eisenstein, David H. Weinberg, Eric Agol, Hiroaki Aihara, Carlos Allende Prieto, Scott F. Anderson, James A. Arns, Eric Aubourg, Stephen Bailey, Eduardo Balbinot, Robert Barkhouser, Timothy C. Beers, Andreas A. Berlind, Steven J. Bickerton, Dmitry Bizyaev, Michael R. Blanton, John J. Bochanski, Adam S. Bolton, Casey T. Bosman, Jo Bovy, Howard J. Brewington, W. N. Brandt, Ben Breslauer, J. Brinkmann, Peter J. Brown, Joel R. Brownstein, Dan Burger, Nicolas G. Busca, Heather Campbell, Phillip A. Cargile, William C. Carithers, Joleen K. Carlberg, Michael A. Carr, Yanmei Chen, Cristina Chiappini, Johan Comparat, Natalia Connolly, Marina Cortes, Rupert A. C. Croft, Luiz N. da Costa, Katia Cunha, James R. A. Davenport, Kyle Dawson, Nathan De Lee, Gustavo F. Porto de Mello, Fernando de Simoni, Janice Dean, Saurav Dhital, Anne Ealet, Garrett L. Ebelke, Edward M. Edmondson, Jacob M. Eiting, Stephanie Escoffier, Massimiliano Esposito, Michael L. Evans, Xiaohui Fan, Bruno Femenia Castella, Leticia Dutra Ferreira, Greg Fitzgerald, Scott W. Fleming, Andreu Font-Ribera, Eric B.

Ford, Peter M. Frinchaboy, Ana Elia Garcia Perez, B. Scott Gaudi, Jian Ge, Luan Ghezzi, Bruce A. Gillespie, G. Gilmore, Leo Girardi, J. Richard Gott, Andrew Gould, Eva K. Grebel, James E. Gunn, Jean-Christophe Hamilton, Paul Harding, David W. Harris, Suzanne L. Hawley, Frederick R. Hearty, Jonay I. Gonzalez Hernandez, Shirley Ho, David W. Hogg, Jon A. Holtzman, Klaus Honscheid, Naohisa Inada, Inese I. Ivans, Linhua Jiang, Peng Jiang, Jennifer A. Johnson, Cathy Jordan, Wendell P. Jordan, Guinevere Kauffmann, Eyal Kazin, David Kirkby, Mark A. Klaene, Jean-Paul Kneib, G. R. Knapp, C. S. Kochanek, Lars Koesterke, Juna A. Kollmeier, Richard G. Kron, Dustin Lang, James E. Lawler, Jean-Marc Le Goff, Brian L. Lee, Young Sun Lee, Jarron M. Leisenring, Yen-Ting Lin, Jian Liu, Daniel C. Long, Craig P. Loomis, Sara Lucatello, Britt Lundgren, Robert H. Lupton, Bo Ma, Zhibo Ma, Nicholas MacDonald, Claude Mack, Suvrath Mahadevan, Marcio A. G. Maia, Elena Malanushenko, Viktor Malanushenko, Steven R. Majewski, Martin Makler, Rachel Mandelbaum, Claudia Maraston, Daniel Margala, Paul Maseman, Karen L. Masters, Cameron K. McBride, Patrick McDonald, Ian D. McGreer, Richard G. McMahon, Olga Mena Requejo, Brice Menard, Jordi Miralda-Escude, Heather L. Morrison, Fergal Mullally, Demitri Muna, Hitoshi Murayama, Adam D. Myers, Tracy Naugle, Angelo Fausti Neto, Duy Cuong Nguyen, Robert C. Nichol, David L. Nidever, Robert W. O'Connell, Ricardo L. C. Ogando, Matthew D. Olmstead, Daniel J. Oravetz, Nikhil Padmanabhan, Martin Paegert, Nathalie Palanque-Delabrouille, Kaike Pan, Parul Pandey, John K. Parejko, Isabelle Paris, Paulo Pellegrini, Joshua Pepper, Will J. Percival, Patrick Petitjean, Robert Pfaffenberger, Janine Pforr, Stefanie Phleps, Christophe Pichon, Matthew M. Pieri, Francisco Prada, Adrian M. Price-Whelan, M. Jordan Raddick, Beatriz H. F. Ramos, Celine Ryle, I. Neill Reid, James Rich, Gordon T. Richards, George H. Rieke, Marcia J. Rieke, Hans-Walter Rix, Annie C. Robin, Helio J. Rocha-Pinto, Constance M. Rockosi, Natalie A. Roe, Emmanuel Rollinde, Ashley J. Ross, Nicholas P. Ross, Bruno Rossetto, Ariel G. Sanchez, Basilio Santiago, Conor Sayres, Ricardo Schiavon, David J. Schlegel, Katharine J. Schlesinger, Sarah J. Schmidt, Donald P. Schneider, Kris Sellgren, Alaina Shelden, Erin Sheldon, Matthew Shetrone, Yiping Shu, John D. Silverman, Jennifer Simmerer, Audrey E. Simmons, Thirupathi Sivarani, M. F. Skrutskie, Anze Slosar, Stephen Smee, Verne V. Smith, Stephanie A. Snedden, Keivan G. Stassun, Oliver Steele, Matthias Steinmetz, Mark H. Stockett, Todd Stollberg, Michael A. Strauss, Masayuki Tanaka, Aniruddha R. Thakar, Daniel Thomas, Jeremy L. Tinker, Benjamin M. Tofflemire, Rita Tojeiro, Christy A. Tremonti, Mariana Vargas Magana, Licia Verde, Nicole P. Vogt, David A. Wake, Xiaoke Wan, Ji Wang, Benjamin A. Weaver, Martin White, Simon

D. M. White, John C. Wilson, John P. Wisniewski, W. Michael Wood-Vasey, Brian Yanny, Naoki Yasuda, Christophe Yeche, Donald G. York, Erick Young, Gail Zasowski, Idit Zehavi, and Bo Zhao. SDSS-III: Massive Spectroscopic Surveys of the Distant Universe, the Milky Way Galaxy, and Extra-Solar Planetary Systems. *The Astronomical Journal*, 142(3):72, September 2011. arXiv: 1101.1529.

[14] Daniel Fabricant, Robert Fata, John Roll, Edward Hertz, Nelson Caldwell, Thomas Gauron, John Geary, Brian McLeod, Andrew Szentgyorgyi, Joseph Zajac, Michael Kurtz, Jack Barberis, Henry Bergner, Warren Brown, Maureen Conroy, Roger Eng, Margaret Geller, Richard Goddard, Michael Honsa, Mark Mueller, Douglas Mink, Mark Ordway, Susan Tokarz, Deborah Woods, William Wyatt, Harland Epps, and Ian Dell'Antonio. Hectospec, the MMT's 300 Optical Fiber-Fed Spectrograph. *Publications of the Astronomical Society of the Pacific*, 117(838):1411–1434, December 2005.

[15] N. Fahim, F. Prada, J. P. Kneib, J. Sánchez, P. Hórler, M. Azzaro, S. Becerril, H. Bleuler, M. Bouri, J. Castano, J. Garrido, D. Gillet, G. Glez-de Rivera, C. Gómez, M. A. Gómez, A. Gonzalez-Arroyo, L. Jenni, L. Makarem, G. Yepes, X. Arrillaga, M. A. Carrera, R. Diego, M. Charif, M. Hug, and C. Lachat. An 8-mm diameter Fiber Robot Positioner for Massive Spectroscopy Surveys. *Monthly Notices of the Royal Astronomical Society*, 450(1):794–806, April 2015. arXiv: 1410.4722.

[16] Charles Fisher, Chaz Morantz, David Braun, Michael Seiffert, Hrand Aghazarian, Eamon Partos, Matthew King, Larry E. Hovland, Mark Schwochert, Joel Kaluzny, Christopher Capocasale, Andrew Houck, Johannes Gross, Daniel Reiley, Peter Mao, Reed Riddle, Khanh Bui, David Henderson, Todd Haran, Robert Culhane, Daniele Piazza, and Eric Walkama. Developing engineering model Cobra fiber positioners for the Subaru Telescope's prime focus spectrometer. volume 9151, pages 91511Y–91511Y–13, 2014.

[17] Charles D. Fisher, David F. Braun, Joel V. Kaluzny, Michael D. Seiffert, Richard G. Dekany, Richard S. Ellis, and Roger M. Smith. Developments in high-density Cobra fiber positioners for the Subaru Telescope's Prime Focus Spectrometer. volume 8450, pages 845017–845017–8, 2012.

[18] Brenna Flaugher and Chris Bebek. The Dark Energy Spectroscopic Instrument (DESI). In *Ground-based and Airborne Instrumentation for Astronomy V*, volume 9147, page 91470S. International Society for Optics and Photonics, July 2014.

[19] Jian Ge, Jiaru Chu, Jianping Wang, Bo Zhao, Hongzhuan Hu, and Yongtian Zhu. A Wide Field Optical Spectrograph Concept for TMT.

[20] James Gilbert, Michael Goodwin, Jeroen Heijmans, Rolf Muller, Stan Miziarski, Jurek Brzeski, Lew Waller, Will Saunders, Alex Bennet, and Julia Tims. Starbugs: all-singing, all-dancing fibre positioning robots. In *SPIE Astronomical Telescopes+ Instrumentation*, pages 84501A–84501A. International Society for Optics and Photonics, 2012.

[21] Peter R. Gillingham, Stan Miziarski, Masayuki Akiyama, and Volker Klocke. Echidna: a multifiber positioner for the Subaru prime focus. In *Astronomical Telescopes and Instrumentation*, pages 1395–1403. International Society for Optics and Photonics, 2000.

[22] Peter R. Gillingham, Anna M. Moore, Masayuki Akiyama, Jurek Brzeski, David Correll, John Dawson, Tony J. Farrell, Gabriella Frost, Jason S. Griesbach, Roger Haynes, and others. The fiber multi-object spectrograph (fmos) project: the anglo-australian observatory role. In *Astronomical Telescopes and Instrumentation*, pages 985–996. International Society for Optics and Photonics, 2003.

[23] Michael Goodwin, Jurek Brzeski, Scott Case, Matthew Colless, Tony Farrell, Luke Gers, James Gilbert, Jeroen Heijmans, Andrew Hopkins, Jon Lawrence, and others. MANIFEST instrument concept and related technologies. In *SPIE Astronomical Telescopes+ Instrumentation*, pages 84467I–84467I. International Society for Optics and Photonics, 2012.

[24] Michael Goodwin, Jeroen Heijmans, Ian Saunders, Jurek Brzeski, Will Saunders, Rolf Muller, Roger Haynes, and James Gilbert. Starbugs: focal plane fiber positioning technology. In *Modern Technologies in Space- and Ground-based Telescopes and Instrumentation*, volume 7739, page 77391E. International Society for Optics and Photonics, July 2010.

[25] Andy Green, Sarah Brough, Angel Lopez-Sanchez, Rob Sharp, Russell Cannon, and Terry Bridges. 2df–AAOmega Manual, August 2014.

[26] Philipp Hörler, Luzius Kronig, Jean-Paul Kneib, Mohamed Bouri, Hannes Bleuler, and Dieter von Moos. High density fiber postitioner system for massive spectroscopic surveys. *Monthly Notices of the Royal Astronomical Society*, 481(3):3070–3082, December 2018.

[27] Masahiko Kimura, Toshinori Maihara, Fumihide Iwamuro, Masayuki Akiyama, Naoyuki Tamura, Gavin B. Dalton, Naruhisa Takato, Philip Tait,

Kouji Ohta, Shigeru Eto, Daisaku Mochida, Brin Elms, Kaori Kawate, Tomio Kurakami, Yuuki Moritani, Junichi Noumaru, Norio Ohshima, Masanao Sumiyoshi, Kiyoto Yabe, Jurek Brzeski, Tony Farrell, Gabriella Frost, Peter R. Gillingham, Roger Haynes, Anna M. Moore, Rolf Muller, Scott Smedley, Greg Smith, David G. Bonfield, Charles B. Brooks, Alan R. Holmes, Emma Curtis Lake, Hanshin Lee, Ian J. Lewis, Tim R. Froud, Ian A. Tosh, Guy F. Woodhouse, Colin Blackburn, Robert Content, Nigel Dipper, Graham Murray, Ray Sharples, and David J. Robertson. Fibre Multi-Object Spectrograph (FMOS) for the Subaru Telescope. *Publications of the Astronomical Society of Japan*, 62(5):1135–1147, October 2010.

[28] Luzius Kronig, Philipp Hörler, Jean-Paul Kneib, and Mohamed Bouri. Design and performances of an optical metrology system to test position and tilt accuracy of fiber positioners. In *Advances in Optical and Mechanical Technologies for Telescopes and Instrumentation III*, volume 10706, page 107066B. International Society for Optics and Photonics, July 2018.

[29] Ian J. Lewis, Gavin B. Dalton, Matthew Brock, James Gilbert, Don C. Abrams, J. Alfonso L. Aguerri, Piercarlo Bonifacio, Kevin Middleton, and Scott C. Trager. Fibre positioning concept for the WEAVE spectrograph at the WHT. page 914734, July 2014.

[30] Laleh Makarem. *Decentralized multi-robot coordination in crowded workspaces*. PhD thesis, EPFL, Lausanne, 2015.

[31] Laleh Makarem, Jean-Paul Kneib, Denis Gillet, Hannes Bleuler, Mohamed Bouri, Philippe Hörler, Laurent Jenni, Francisco Prada, and Justo Sánchez. Collision-free motion planning for fiber positioner robots: discretization of velocity profiles. volume 9152, pages 91520Q–91520Q–10, 2014.

[32] Reed D. Meyer, Kevin J. Kearney, Zoran Ninkov, Christopher T. Cotton, Peter Hammond, and Bryan D. Statt. RITMOS: a micromirror-based multi-object spectrometer. In *Ground-based Instrumentation for Astronomy*, volume 5492, pages 200–220. International Society for Optics and Photonics, September 2004.

[33] Anna M. Moore, Peter R. Gillingham, Jason S. Griesbach, and Masayuki Akiyama. Spine development for the Echidna fiber positioner. In *Astronomical Telescopes and Instrumentation*, pages 1429–1439. International Society for Optics and Photonics, 2003.

[34] Luca Pasquini, B. Delabre, R. Ellis, and Tim de Zeeuw. New telescope designs suitable for massively multiplexed spectroscopy. In *Ground-based and*

Airborne Telescopes VI, volume 9906, page 99063C. International Society for Optics and Photonics, July 2016.

[35] Claire Poppett, Ray Sharples, Jerry Edelstein, Jurgen Schmoll, and David Bramall. The DESI fiber system. In *Ground-based and Airborne Instrumentation for Astronomy VII*, volume 10702, page 107027O. International Society for Optics and Photonics, July 2018.

[36] Lawrence W. Ramsey. Focal ratio degradation in optical fibers of astronomical interest. volume 3, pages 26–39, 1988.

[37] Massimo Robberto, Megan Donahue, Zoran Ninkov, Stephen A. Smee, Robert H. Barkhouser, Mario Gennaro, and Andrei Tokovinin. SAMOS: a versatile multi-object-spectrograph for the GLAO system SAM at SOAR. In *Ground-based and Airborne Instrumentation for Astronomy VI*, volume 9908, page 99088V. International Society for Optics and Photonics, August 2016.

[38] Will Saunders, Scott Smedley, Peter Gillingham, Jaime E. Forero-Romero, Stephanie Jouvel, and Brian Nord. Target allocation yields for massively multiplexed spectroscopic surveys with fibers. In *SPIE Astronomical Telescopes+ Instrumentation*, pages 915023–915023. International Society for Optics and Photonics, 2014.

[39] Will Saunders, Greg Smith, James Gilbert, Rolf Muller, Michael Goodwin, Nick Staszak, Jurek Brzeski, Stan Miziarski, and Matthew Colless. 'MOHAWK: a 4000-fiber positioner for DESpec. In *SPIE Astronomical Telescopes+ Instrumentation*, pages 84464W–84464W. International Society for Optics and Photonics, 2012.

[40] Allar Saviauk, Frank Dionies, Roelof de Jong, Roger Haynes, and Ian Parry. The fiber positioner for 4most: exploration of an alternative R-θ design. In *Advances in Optical and Mechanical Technologies for Telescopes and Instrumentation*, volume 9151, page 91514Y. International Society for Optics and Photonics, July 2014.

[41] Frédéric Sayède, Isabelle Guinouard, Gilles Fasola, Emilie Lhome, Jean-Philippe Amans, Piercarlo Bonifacio, Don Carlos Abrams, Kevin Middleton, Gavin Dalton, J. Alfonso L. Aguerri, Scott C. Trager, and Avi Loeb. WEAVE MOS fibre bundle test plan. In *Advances in Optical and Mechanical Technologies for Telescopes and Instrumentation*, volume 9151, page 91515Y. International Society for Optics and Photonics, July 2014.

[42] O. Scaglione, M. Markovic, and Y. Perriard. Extension of the local observability down to zero speed of BLDC motor state-space models using iron B-H

local hysteresis. In *2011 International Conference on Electrical Machines and Systems*, pages 1–4, August 2011.

[43] Michael Schubnell, Jon Ameel, Robert W. Besuner, Irena Gershkovich, Philipp Hoerler, Jean-Paul Kneib, Henry D. Heetderks, Joseph H. Silber, Gregory Tarlé, and Curtis Weaverdyck. The DESI fiber positioner system. In *Ground-based and Airborne Instrumentation for Astronomy VI*, volume 9908, page 990892. International Society for Optics and Photonics, August 2016.

[44] Joseph H. Silber, Christoph Schenk, Eric Anderssen, Chris Bebek, Frederic Becker, Robert Besuner, Mario Cepeda, Jerry Edelstein, Henry Heetderks, Patrick Jelinsky, Thomas Johnson, Armin Karcher, Paul Perry, Rodney Post, Michael Sholl, Kenneth Wilson, and Zengxaing Zhou. Design and performance of an R-theta; fiber positioner for the BigBOSS instrument. volume 8450, pages 845038–845038–13, 2012.

[45] Peter Spanoudakis, Laurent Giriens, Simon Henein, Leszek Lisowski, Aidan O'Hare, Emmanuel Onillon, Philippe Schwab, and Patrick Theurillat. Configurable slit-mask unit of the Multi-Object Spectrometer for Infra-Red Exploration for the Keck telescope: Integration and Tests - art. no. 701801. 7018, July 2008.

[46] Masahiro Takada, Richard S. Ellis, Masashi Chiba, Jenny E. Greene, Hiroaki Aihara, Nobuo Arimoto, Kevin Bundy, Judith Cohen, Olivier Doré, Genevieve Graves, James E. Gunn, Timothy Heckman, Christopher M. Hirata, Paul Ho, Jean-Paul Kneib, Olivier Le Fèvre, Lihwai Lin, Surhud More, Hitoshi Murayama, Tohru Nagao, Masami Ouchi, Michael Seiffert, John D. Silverman, Laerte Sodré, David N. Spergel, Michael A. Strauss, Hajime Sugai, Yasushi Suto, Hideki Takami, and Rosemary Wyse. Extragalactic science, cosmology, and Galactic archaeology with the Subaru Prime Focus Spectrograph. *Publications of the Astronomical Society of Japan*, 66(1), February 2014.

[47] Xiaozheng Xing, Chao Zhai, Huasheng Du, Weimin Li, Hongzhuan Hu, Ruifang Wang, and Dexiu Shi. Parallel controllable optical fiber positioning system for LAMOST. volume 3352, pages 839–849, 1998.

[48] Gang Zhao, Yong-Heng Zhao, Yao-Quan Chu, Yi-Peng Jing, and Li-Cai Deng. LAMOST spectral survey—An overview. *Research in Astronomy and Astrophysics*, 12(7):723, 2012.

Philipp Hörler
Ch. Des Osches 73
1009 Pully
+41 76 822 47 30
philipp.horler@gmail.com

30 years, Swiss

Mechanical engineer EPFL

SKILLS

- Mechanical design
- Electric motor control
- Test bench development

- Micro-robotics
- High-precision mechanics
- Astronomical instrumentation

EDUCATION

2014-2018 **PhD in robotics – EPFL,** laboratoire de systèmes robotiques

Development of micro-robotic systems for high-precision positioning in astronomical telescopes
- Mechanical design of micro-robotic positioners
- Development of drive electronics and firmware
- Development of a test bench for high precision positioning (1µm) and tilt (0.01°) measurements
- Realization and testing of prototypes
- Working in international collaborations (DESI, MOONS, SDSS-V)

2011-2012 **Master in mechanical engineering – EPFL**
- Identification and control of dynamic systems
- Mechanical design

2006-2009 **Bachelor in mechanical engineering – EPFL**

PROFESSIONAL EXPERIENCES

2013-2014 **Scientific collaborator – EPFL,** laboratoire de systèmes robotiques
7 months   Development of micro-robotic systems for high-precision positioning in astronomical instruments

2011-2013 **Civil service – Vaud University Hospital (CHUV)**, department of nuclear medicine
6 months   Statistical studies of medical images, development of software tool for operations

2010   **Engineering internship – B&G Ingénieurs Conseils**
4 months   Technical and economic feasibility studies for transport systems

2007-2018 **Teaching – EPFL**
- Assistantships: Electrotechnics, Robotics, Physics, Programming (C++), MATLAB, LabVIEW
- Supervision of semester projects: micro-robotic positioners, micro-gearheads

2008   **Industrial internship – Jörimann Stahl AG**
1 month   Manufacturing and assembly of machines for tunnel constructions

IT SKILLS

CAD	**CATIA, Solidworks, Abaqus, Flux**
Engineering tools	**MATLAB, Simulink, LabVIEW**
Programming	**C, C++, Python**
Office tools	**Suite Office, Suite Google, LaTeX**

LANGUAGES

German (Swiss)	mother tongue
French	C2
English	C2
Italian	B1-B2